

DETECTION OF CO HOTSPOTS ASSOCIATED WITH YOUNG CLUSTERS IN THE SOUTHERN STARBURST GALAXY NGC 1365

KAZUSHI SAKAMOTO^{1,2}, PAUL T. P. HO^{3,4}, RUI-QING MAO⁵,
SATOKI MATSUSHITA⁴, AND ALISON B. PECK¹

Accepted for publication in ApJ

ABSTRACT

We have used the Submillimeter Array for the first interferometric CO imaging toward the starburst-Seyfert nucleus of the southern barred spiral galaxy NGC 1365, which is one of the four galaxies within 30 Mpc that have $L_{8-1000\ \mu\text{m}} \geq 10^{11} L_{\odot}$. Our mosaic maps of ^{12}CO , ^{13}CO , and $\text{C}^{18}\text{O}(J=2-1)$ emission at up to $2''$ (200 pc) resolutions have revealed a circumnuclear gas ring and several CO clumps in the central 3 kpc. The molecular ring shows morphological and kinematical signs of bar-driven gas dynamics, and the region as a whole is found to follow the star formation laws of Kennicutt. We have found that some of the gas clumps and peaks in CO brightness temperature, which we collectively call CO hotspots, coincide with the radio and mid-infrared sources previously identified as dust-enshrouded super star clusters. This hotspot-cluster association suggests that either the formation of the most massive clusters took place in large molecular gas concentrations (of $\Sigma_{\text{mol}} \sim 10^3 M_{\odot} \text{pc}^{-2}$ in 200 pc scales) or the clusters have heated their ambient gas to cause or enhance the CO hotspots. The active nucleus is in the region of weak CO emission and is not associated with distinctive molecular gas properties.

Subject headings: galaxies: starburst — galaxies: ISM — galaxies: star clusters — galaxies: active — galaxies: individual (NGC 1365)

1. INTRODUCTION

Central regions of spiral galaxies sometimes host vigorous star formation called (circum)nuclear starbursts. This phenomenon forms stars at a higher rate and more preferentially in compact massive clusters than a non-starburst environment (e.g., Telesco et al. 1993; Barth et al. 1995). Since stars form from molecular gas, properties of the molecular gas are expected to control the starbursts. The study of such properties in nearby starbursts tells us about physical processes involved in the phenomenon, and the information serves as a basis for modeling starbursts throughout galaxy evolution.

The typical extent of a (circum)nuclear starburst in our vicinity is $\lesssim 1$ kpc, which is only $20''$ for a distance of 10 Mpc. High angular resolution is therefore essential for starburst studies. In particular, high resolution imaging of molecular gas with millimeter interferometers has been a powerful tool in the field (e.g., Jogee et al. 2005). Until very recently, however, such arrays had been operated only at the mid-latitudes in the northern hemisphere, leaving many southern galaxies unattainable.

We have now observed NGC 1365, a starburst-Seyfert composite galaxy in the southern sky, using the Submillimeter Array (SMA)⁶. This is part of our SMA survey of southern starbursts, aiming to explore molecular gas and dust in some of

the most important but undeservedly less observed starburst galaxies in the southern sky. NGC 1365 is one of our targets because it has the circumnuclear starburst typical of barred spirals, and because the infrared luminosity of the starburst is among the largest in non-merging galaxies, bridging more luminous starbursts in distant mergers and less luminous ones in undisturbed spirals. Other galaxies reported so far from our survey are M83, NGC 253, and NGC 3256 (Sakamoto et al. 2004, 2006a,b).

We have observed CO emission to trace the molecular gas. Our resolution of $2''$ is a significant improvement over the best previous ones of $5''-10''$. In addition, the three isotopic lines that were simultaneously imaged, i.e., the $J=2-1$ transitions of ^{12}CO , ^{13}CO , and C^{18}O , provide information about the physical properties of the molecular gas. Among other things, we have discovered bright CO spots, or CO hotspots, that are associated with young massive star clusters in the starburst. We discuss their properties and relation to the starburst.

The goals of this paper are (1) to report the detailed structure, kinematics, and properties of molecular gas in the central region of NGC 1365 on the basis of the new high-resolution data, (2) to search for the relation between circumnuclear starburst and the gas properties, and (3) to see if there is anything special in the molecular gas in the vicinity of the Seyfert nucleus. The next section further introduces NGC 1365, and §3 describes our SMA observations and data reduction. The observational results are presented in §4, and are discussed in §5 – §7. A summary is given in §8.

2. NGC 1365

NGC 1365 is an archetype of barred spiral galaxies and hosts a circumnuclear starburst and a Seyfert nucleus. A comprehensive review of the galaxy is given in Lindblad (1999). A short summary of the properties of this galaxy is provided below and in Table 1. We adopt a Cepheid-based distance of 17.95 Mpc (Freedman et al. 2001). At this distance, $1''$ corresponds to 86 pc and 1 kpc to $11''5$. The galaxy has a long

¹ Harvard-Smithsonian Center for Astrophysics, Submillimeter Array, 645, N. A'ohoku Place, Hilo, HI 96720

² National Astronomical Observatory of Japan, Mitaka, Tokyo 181-8588, Japan. email: sakamoto.kazushi@nao.ac.jp

³ Harvard-Smithsonian Center for Astrophysics, 60 Garden Street, Cambridge, MA 02138

⁴ Academia Sinica, Institute of Astronomy and Astrophysics, P.O. Box 23-141, Taipei 106, Taiwan

⁵ Purple Mountain Observatory, Chinese Academy of Sciences, Nanjing, 210 008, China

⁶ The Submillimeter Array is a joint project between the Smithsonian Astrophysical Observatory and the Academia Sinica Institute of Astronomy and Astrophysics, and is funded by the Smithsonian Institution and the Academia Sinica.

stellar bar, spanning about $3'$ on the sky (Regan & Elmegreen 1997) or 18 kpc on the galaxy plane. The bar has a pair of dust lanes in its front edge, assuming that the spiral arms are trailing in the galaxy. The assumption makes the northwest side of the galaxy near to us. The dust lanes curve inward near the galactic center to suggest an oval ring around the nucleus (see, e.g., the optical images in NED).

Active star formation in the circumnuclear region was first noticed as optical hotspots by Morgan (1958) and Sersic & Pastoriza (1967). Later optical imaging using the Hubble Space Telescope (HST) revealed dozens of bright compact clusters around the dust ring (Kristen et al. 1997). The brightest of them, after extinction correction, is 300 times brighter than the most luminous globular cluster in our Galaxy. Mid-IR ($10\text{--}13\ \mu\text{m}$) imaging by Galliano et al. (2005) also revealed several compact sources, presumably compact clusters, in the region. These clusters have been identified as the so-called super star clusters, or young clusters as massive as $\sim 10^6 M_{\odot}$ containing thousands of OB stars. The infrared luminosity of NGC 1365 is $L_{8\text{--}1000\ \mu\text{m}} = 10^{11.00} L_{\odot}$ (Sanders et al. 2003), which makes it one of only four objects having $\geq 10^{11} L_{\odot}$ within 30 Mpc⁷. At $15\ \mu\text{m}$, 71% of the total flux of the galaxy originates from within the central $43''$ (Roussel et al. 2001). Thus most of the infrared luminosity probably comes from inside the starburst region of less than 2 kpc radius.

In the radio, where dust obscuration is minimal, a circumnuclear ring of about $20'' \times 9''$ containing several compact ($< 1''$) peaks have been found at 2–20 cm (Sandqvist et al. 1982, 1995; Saikia et al. 1994; Forbes & Norris 1998; Morganti et al. 1999; Thean et al. 2000). Some of the radio and the mid-IR sources coincide. The brightest radio hotspots have a power of $P_{6\text{cm}} \sim 10^{20}\ \text{W Hz}^{-1}$ for each. In other words, they are more than 100 times as luminous as Cas A, are comparable to the brightest radio sources in M82 and NGC 253 (Kronberg et al. 1985; Ulvestad & Antonucci 1997), and are also comparable in radio power with radio supernovae (Weiler et al. 2002). The center of the galaxy is also bright in molecular lines (e.g., Sandqvist et al. 1995, 1999). Previous observations found bar-driven twin peaks of molecular gas in the region (Sandqvist et al. 1999; Ott et al. 2005), and higher resolution observations fully resolving the gas structure have been needed.

The Seyfert 1.5 nucleus of the galaxy is the driver, or at least the ionizing source, of a biconical plasma outflow (Phillips et al. 1983; Kristen et al. 1997; Veilleux et al. 2003), but the AGN is of low-luminosity and a small contributor to the luminosity of the central region (Iyomoto et al. 1997; Komossa & Schulz 1998; Stevens et al. 1999). The mid- and far-IR spectral indexes of the galaxy, $\alpha(60, 25) = -2.2$ and $\alpha(100, 60) = -1.1$ for $S_{\lambda} \propto \lambda^{-\alpha}$ and the IRAS fluxes in Sanders et al. (2003), are not those of ‘warm’ AGN-dominated sources but those of H II-type galaxies (de Grijp et al. 1985; Miley et al. 1985). The position of the nucleus in Table 1 is the average of optical, near-IR, and radio positions. We use it as a coordinate reference for observations without accurate astrometry.

3. SMA OBSERVATIONS AND DATA REDUCTION

NGC 1365 was observed using the Submillimeter Array on the 4100 m summit of Mauna Kea, Hawaii. The array consists

of eight 6-meter antennas, cryogenically cooled SIS receivers, and digital correlators. More information on the array is presented in Ho et al. (2004). Parameters of our observations are summarized in Table 2.

Two nights of observations were made in the 2003–2004 winter with the array in its compact and extended configurations. The SIS receivers were tuned to simultaneously detect three CO lines in the 1 mm band, namely $^{12}\text{CO}(2\text{--}1)$ in the upper sideband (USB) and $^{13}\text{CO}(2\text{--}1)$ and $\text{C}^{18}\text{O}(2\text{--}1)$ in the lower sideband (LSB). The digital correlators have a 2 GHz bandwidth in each sideband and were configured for a spectral resolution of 0.8125 MHz. The southern galaxy was observed between the elevations of 15° and 34° under excellent weather with zenith opacity of 0.05–0.08. The median double-sideband system temperature toward the galaxy was 210 K and 160 K for each night. After flagging bad scans, the galaxy data have projected baselines in the range of 6.8 – 175.0 m and the total integration time of 6.5 hr.

We made mosaics with a half-power field of view of about $100'' \times 50''$ by observing three positions, namely the galactic center and two offset positions $25''$ from the center along the position angle of 70° . They were cycled every 12 minutes to give similar $u\text{--}v$ coverage for each position. We also observed quasars J0132–169 and J0457–234 for gain calibration, Jupiter, Saturn, Uranus, Callisto, Ganymede, 3C279, and J2258–279 for passband calibration, and used Mars and Uranus for flux calibration⁸. A small correction, 7% in amplitude, is made to our data to compensate for the lack of automatic focus tracking at the time of the observations (Matsushita et al. 2006).

The SMA data were reduced in three steps. First, the standard passband and gain calibrations were made using MIR, which is an IDL version of MMA (Scoville et al. 1993). Then mosaic images were made from the calibrated visibilities using MIRIAD (Sault et al. 1995). Finally, the NRAO AIPS package (Bridle & Greisen 1994) was used for data analysis. In the imaging process, the spectral-line data were binned to $10\ \text{km s}^{-1}$ or $20\ \text{km s}^{-1}$ resolutions and various types of $u\text{--}v$ weighting were employed. For one set of images, each line was given a different $u\text{--}v$ weighting (i.e., **robust** value) in order to maximize spatial resolution while retaining reasonable signal-to-noise ratio. For another, we used exactly the same range of $u\text{--}v$ radii and the same $u\text{--}v$ weighting for different lines in order to accurately measure line intensity ratios. Continuum data were made by combining channels without line emission, and the total bandwidth of the data was 0.7 GHz in each sideband. Weak continuum emission was detected at about 5σ . The continuum was subtracted from the line data in the $u\text{--}v$ domain.

We compared our data with previous single-dish observations to check consistency. Fig. 1 shows the CO spectra to be compared with $25''$ resolution observations at the galactic center. They are made from the data cubes used for Fig. 2. The asymmetry of the line profile seen in all the lines, with stronger blue-shifted emission, is due to an intrinsic asymmetry of gas distribution. The total flux in each line is $5.5 \times 10^3\ \text{Jy km s}^{-1}$, $4.1 \times 10^2\ \text{Jy km s}^{-1}$, and $1.1 \times 10^2\ \text{Jy km s}^{-1}$ for $^{12}\text{CO}(2\text{--}1)$, $^{13}\text{CO}(2\text{--}1)$, and $\text{C}^{18}\text{O}(2\text{--}1)$, respectively. Sandqvist et al. (1995) observed the same position in $^{12}\text{CO}(2\text{--}1)$ with a $25''$ beam at the Swedish-ESO-Submillimeter Telescope (SEST) and obtained a total flux of

⁷ The other three are NGC 1068, a merger NGC 2146, and NGC 7552 at $\delta = -42^{\circ}$.

⁸ Mars was not used in the USB because of the significant ^{12}CO absorption in the sideband.

$4.9 \times 10^3 \text{ Jy km s}^{-1}$. Thus the SMA and SEST observations agree with each other considering that each probably has an uncertainty of $\sim 10\%$. The SEST line profile has a symmetric double peak unlike SMA's, and the small pointing offset implied by this may be a part of the reasons for the smaller SEST flux. We conclude from the comparison that the SMA observations detected most of the CO flux in the galactic center. We also infer that our $^{13}\text{CO}(2-1)$ and $\text{C}^{18}\text{O}(2-1)$ data similarly detected most of the flux in the observed area because they have almost the same $u-v$ coverage as the $^{12}\text{CO}(2-1)$ data and because the $u-v$ weighting used for them are closer to the natural weighting.

In this paper, velocities are with respect to the Local Standard of Rest (LSR) and are defined in the radio convention. Maps are presented without correcting for the attenuation by the mosaicked primary beam, unless otherwise noted. However, all the flux and intensity measurements are made after the correction. Line spectra are also made from data cubes after the correction.

4. RESULTS

4.1. Gas Distribution

The CO maps in Figure 2 show that the emission is mostly in the central $4 \times 2 \text{ kpc}$ of our $9 \times 5 \text{ kpc}$ field of view and that brighter emission is on an elliptical ring. There are gas lanes on the leading sides of the bar which curve inward near the nucleus to form the incomplete circumnuclear ring. This gas morphology agrees with that of dust lanes seen in the optical (Fig. 3), except in its western part (i.e., the near side) where only the dark lane is conspicuous. The oval ring has a major axis of about 2 kpc ($\sim 20''$), is made of several distinct gas clumps, and is surrounded by weaker emission. Particularly in the rare CO isotopes, a pair of condensations stands out near the ring's apocenters, where the ring and leading-edge gas lanes connect. This feature, resembling the gas 'twin-peaks' observed in the centers of many barred galaxies (Kenney et al. 1992), is the one previously observed in $\text{CO}(3-2)$ and NH_3 (Sandqvist et al. 1999; Ott et al. 2005). The $\text{CO}(2-1)$ emission does not peak at the Seyfert nucleus. The 1.3 mm continuum is detected at about 5σ near the brighter one of the twin peaks.

Radial distribution of the ^{12}CO integrated intensity, sampled in concentric circular rings in the galaxy plane and shown in Figure 4, confirms the molecular ring and the compact size of the central gas concentration. The peak at the radius of about $5''$ is due to the ring smeared by the circular sampling. The radial profile rapidly declines outwards, falling to $1/10$ of the peak at a radius of 2 kpc ($23''$). The extent of this molecular gas concentration is comparable to that of dust emission at 7 and $15 \mu\text{m}$ and that of ionized gas seen at 3 and 6 cm (Roussel et al. 2001; Forbes & Norris 1998). The warm dust and hot gas reflect the active star formation in the region.

The mass of molecular gas in the galactic center is estimated using a conversion factor from ^{12}CO integrated intensity to H_2 column density, $X_{\text{CO}} = 0.5 \times 10^{20} \text{ cm}^{-2} (\text{K km s}^{-1})^{-1}$. The adopted coefficient is a middle value of the empirical estimates for the center of our Galaxy (Sodroski et al. 1995; Oka et al. 1998; Strong et al. 2004), and is about a factor of 3–6 smaller than the ones estimated for the disk of our Galaxy (e.g. Sanders et al. 1984; Hunter et al. 1997; Dame et al. 2001). The tendency for a galactic center, especially a starburst nucleus, to have a lower conversion factor than the Galactic disk has been suggested by a number of authors (e.g. Maloney & Black 1988;

Bryant & Scoville 1996; Meier & Turner 2001). We also assume that the scaling factor is constant over the region we observed, and that the $^{12}\text{CO}(1-0)$ and $^{12}\text{CO}(2-1)$ lines have the same brightness temperature. Single-dish observations of the $2-1$ to $1-0$ ratio range from 0.55 to 1.1 for the galactic center (Sandqvist et al. 1988, 1995; Papadopoulos & Seaquist 1998; Curran et al. 2001). The latter approximation makes $X_{\text{CO}(2-1)} = X_{\text{CO}(1-0)}$, and hence we omit the transition index. For brevity, X_{CO} in units of $10^{20} \text{ cm}^{-2} (\text{K km s}^{-1})^{-1}$ is written as x_{CO} in the following; we adopted $x_{\text{CO}} = 0.5$. The $^{12}\text{CO}(2-1)$ flux within a 1 kpc radius of the galactic center in the galaxy plane is $4.3 \times 10^3 \text{ Jy km s}^{-1}$. The mass of molecular gas in the central 2 kpc is thus estimated to be $M_{\text{mol}}(r_g < 1 \text{ kpc}) = 9 \times 10^8 M_{\odot}$ from the above assumptions, the $^{12}\text{CO}(2-1)$ flux, and a factor of 1.36 for the contribution of helium. Molecular mass as a function of radius is in Figure 4.

An alternative way to estimate the mass of molecular gas uses the CO isotope lines that are probably optically thin. The molecular mass in the central 2 kpc is estimated to be $4 \times 10^8 M_{\odot}$ from the $\text{C}^{18}\text{O}(2-1)$ flux of $1.1 \times 10^2 \text{ Jy km s}^{-1}$ in the region. For this, we used the C^{18}O abundance of $[\text{H}_2/\text{C}^{18}\text{O}] = 10^{6.3}$, i.e., $[\text{H}_2/^{12}\text{CO}] = 10^4$ and $[^{12}\text{CO}/\text{C}^{18}\text{O}] = 200$ (Henkel & Mauersberger 1993; Wilson & Rood 1994), and $N(\text{C}^{18}\text{O})/I_{\text{C}^{18}\text{O}(2-1)} \approx 10^{14.6} \text{ cm}^{-2} (\text{K km s}^{-1})^{-1}$ suitable for warm and moderately dense gas ($T_{\text{kin}} > 40 \text{ K}$, $N_{\text{H}_2} = 10^3\text{--}10^{5.5} \text{ cm}^{-3}$, and $\tau(\text{C}^{18}\text{O}2-1) < 0.1$: Stutzki & Güsten 1990; Wild et al. 1992). This estimate uses the fact that CO molecules can be excited only to a limited number of levels for the density and, in that circumstance, the level population becomes independent of temperature when the gas is warm enough. If one instead assumes the LTE, then the mass is the same for 20 K gas and larger for warmer gas. The gas mass from C^{18}O is about a factor of 2 smaller than the one from ^{12}CO . This may mean that the adopted X_{CO} is too large. However, it is also possible that there is lower density gas between or in the outskirts of the molecular clouds, and that C^{18}O can not reliably trace such gas because of difficulty in excitation or lower abundance of the molecule in the thin gas. For the Galactic center, Dahmen et al. (1998) estimated the abundance of this type of thin, invisible, molecular gas to be as much as the C^{18}O -visible gas. We therefore estimate gas mass from ^{12}CO and the abovementioned X_{CO} through the paper. For completeness, the ^{13}CO flux of $3.8 \times 10^2 \text{ Jy km s}^{-1}$ in the region gives a M_{mol} of $3 \times 10^8 M_{\odot}$ for $[^{12}\text{CO}/^{13}\text{CO}] = 40$. The line is more prone to saturate than C^{18}O , and hence the mass is more likely an underestimate. The mass-related and other key parameters measured or estimated from our data are summarized in Table 3.

The uncertainty in the mass estimates is dominated by that in the CO flux-to-mass conversion and may be as large as a factor of a few. It is much larger than the $\sim 10\%$ error in the CO flux. Though we took the center of our Galaxy as a template for our mass estimate, it is quite possible that the scaling relation is offset in the starburst nucleus of NGC 1365. The rare CO isotopes give us an independent check, and the estimate of the error. Note that the scaling factor can plausibly have local scatter within the galactic center, because gas properties are not expected to be uniform throughout the region. It is only the lack of observational information sufficient to locally determine the gas mass, and the scaling relation, that led us to use the constant conversion factor.

Bearing the abovementioned caveats in mind, we can calculate the mass and surface density of molecular gas in small

regions. Figure 5 shows the distribution of CO integrated intensity and molecular surface density in the circumnuclear region. The maximum integrated intensity of $42 \text{ Jy km s}^{-1} \text{ arcsec}^{-2}$ translates to the mass surface density of molecular gas $\Sigma_{\text{mol}} = 9 \times 10^2 M_{\odot} \text{ pc}^{-2}$ in the galaxy plane. The surface density is averaged in our beam having $5.1 \times 10^4 \text{ pc}^2$ area in the plane. The peak is at a compact gas clump $7''$ north of the nucleus. The total mass of molecular gas in the clump is $\sim 5 \times 10^7 M_{\odot}$. We see later that the gas clump coincides with a prominent radio and mid-IR source called D/M4.

4.2. Kinematics

The velocity field shown in Fig. 2 indicates the presence of noncircular motion, most easily seen as the curved (S-shaped) velocity contours around the systemic velocity. The noncircular motion is, however, rather systematic. The contours show a $m = 2$ symmetry, i.e., they can be rotated by 180° without breaking the overall pattern of the velocity field.

The CO velocity field was fitted with the AIPS task GAL to derive kinematical parameters; integrated intensity was used for data weighting. The large noncircular motion and the limited spatial coverage of the CO data preclude us from determining the inclination and the position angle of the major axis. Hence we adopt those parameters from HI observations of the entire galaxy by Jörsäter & van Moorsel (1995). We expect, however, that the systemic velocity and the dynamical center of the galaxy are little biased by the symmetric noncircular motion. The systemic velocity of the galaxy is estimated as $V_{\text{sys}}(\text{radio, LSR}) = 1618 \text{ km s}^{-1}$ from the fit, and the dynamical center of the galaxy is estimated to be $\alpha = 03^{\text{h}}33^{\text{m}}36.^{\text{s}}35$, $\delta = -36^{\circ}08'25''.8$ (J2000). The position coincides with the Seyfert nucleus within $0''.4$, well within the measurement errors of the dynamical center and the active nucleus.

The major-axis position-velocity (PV) diagram of $^{12}\text{CO}(2-1)$ emission in Figure 6 shows that the molecular ring is around the turnover of the rotation velocity and that no anomalous velocity is observed at the active nucleus. The rotation velocity at the galactocentric radius of 1 kpc ($11''.5$) is approximately 150 km s^{-1} , according to the PV diagram. For the adopted inclination of 40° , the orbital period at the radius and the dynamical mass within the radius are $T_{\text{dyn}}(R_g = 1 \text{ kpc}) \sim 3 \times 10^7 \text{ yr}$ and $M_{\text{dyn}}(R_g \leq 1 \text{ kpc}) \sim 1 \times 10^{10} M_{\odot}$, respectively. Formal errors in these values can not be properly determined without modeling noncircular motion of gas in the nonaxisymmetric potential. For a $\pm 20\%$ uncertainty in the rotation velocity, which we assume to be reasonable for our data, the fractional uncertainties in T_{dyn} and M_{dyn} are $\pm 20\%$ and $\pm 40\%$, respectively. The gas-to-dynamical mass ratio in the central 2 kpc is ~ 0.1 .

4.3. Line Ratios

The ratio of brightness temperatures is measured between $^{12}\text{CO}(2-1)$ and $^{13}\text{CO}(2-1)$ lines in data cubes of matching spatial and velocity resolutions. The line ratio should reflect physical parameters of the molecular gas such as density and column density (e.g., Meier & Turner 2004), and the SMA enables us to accurately measure it at high spatial resolutions through simultaneous observations of the CO lines. Care was taken to make the reduction procedures for the two lines as close as possible. We used visibilities in the range of $u-v$ radii $5\text{--}128 \text{ k}\lambda$ where both lines have data. The same weighting parameter, i.e., a robust value of 0.5, and the same velocity binning, 20 km s^{-1} , were used. The resulting data cubes, which

had slightly different resolutions, were convolved to the same resolution of $3''.3 \times 2''.0$. The line brightness temperatures were sampled in each velocity channel in a grid of $1''.2$ spacing, which is close to the Nyquist frequency for the spatial resolution of the data. The line ratio is calculated only at the (α, δ, ν) pixels where both lines are detected above 3σ .

Figure 7 shows the scatter diagram of the line intensities and the histogram of the $^{12}\text{CO}(2-1)$ to $^{13}\text{CO}(2-1)$ intensity ratio, $R_{12/13}^{(2-1)} \equiv I(^{12}\text{CO } 2-1)/I(^{13}\text{CO } 2-1)$, where $I(\text{line}) \equiv \int T_{\text{b}}(\text{line}) dv$. The ratio $R_{12/13}^{(2-1)}$ is mostly in the range of 4–14; 92% of the data are in this range. The mean and the standard deviation of $R_{12/13}^{(2-1)}$ are 8.7 and 2.8, respectively. The former is consistent with the single-dish measurement of $R_{12/13}^{(2-1)} = 10 \pm 2$ in the central $21''$ of the galaxy (Papadopoulos & Seaquist 1998). The latter is an upper limit of the intrinsic variation of the ratio because of the noise in the data. Small number of pixels having extreme ratios are likely due to noise. In particular, pixels having $R_{12/13}^{(2-1)} \leq 2$, which are less than 2% of the data, are almost certainly noise judging from their mostly isolated locations in the channel maps.

The spatial distribution of the ratio $R_{12/13}^{(2-1)}$ is shown in Figure 8. For this map, line ratios are averaged at each position if there are multiple velocity channels with a valid ratio. The overall trend in the map is that the ratio is relatively high at the ridges of molecular gas. Specifically, higher ratios are seen on the southern molecular ridge at the southern dust lane in the bar, on the southeastern half of the molecular ring, and on the northern molecular ridge in the bar. Lower ratios are mainly observed in the northwestern half of the circumnuclear ring and inside the ring. The $^{12}\text{CO}(2-1)$ to $\text{C}^{18}\text{O}(2-1)$ ratio has the same trend, as seen from the comparison of Figures 2 (a) and 2 (e). Another way to describe the spatial distribution of the line ratio is that there is a trend of the ratio being higher on the far (SE) side than the near (NW) side in the circumnuclear disk of 1 kpc radius (see Figs. 7 and 8). The mean and standard deviation of $R_{12/13}^{(2-1)}$ are (mean $\pm \sigma$) = 7.9 ± 2.2 for the near side and 10.0 ± 2.6 for the far side. A similar trend of higher $R_{12/13}$ in the far side has been noticed in the circumnuclear regions of IC 342 and NGC 253 (Meier & Turner 2001; Sakamoto et al. 2006a), but the illumination model proposed for them may not apply to NGC 1365. This is because the starburst ring coincident with the molecular ring can not preferentially illuminate the side of clouds facing us, nor is there a radial gradient of $R_{12/13}$ expected from AGN illumination. We further discuss the ratio in §6.

4.4. Comparison of CO with Radio and mid-IR sources

We show in Figure 9 the locations and conventional names of the compact radio sources, luminous mid-IR sources, and three of the optically identified super clusters in the circumnuclear region. The radio sources have alphabet names, and the mid-IR sources are called M#, where # is a number. As seen in the figure, some of the radio and mid-IR sources coincide with each other, and are thought to be the same objects, likely young massive clusters embedded in dust (Sandqvist et al. 1995; Galliano et al. 2005). In contrast, the mid-IR sources M2 and M3 do not have a radio counterpart but coincide with optically identified clusters called SSC 3 and SSC 6, respectively, which Kristen et al. (1997) found to be the brightest optical sources in the region except the nucleus. Their mid-IR colors suggest less dust emission than toward other sources

(Galliano et al. 2005), consistent with their optical detection.

Our CO data are compared with the radio and the mid-IR sources in Figure 10. We have produced for the comparison peak brightness temperature maps in addition to the CO integrated intensity maps. Since the peaks in these maps often coincide, we collectively call the peaks CO hotspots. In the maps, radio sources are plotted as squares at average positions of previous observations⁹, while mid-IR sources are marked as crosses.

The comparison shows that some of the radio peaks and mid-IR sources coincide with CO hotspots, i.e., peaks of CO integrated intensity or CO brightness temperature or both. Specifically, the sources D/M4, E/M5, G/M6, and H have a local maximum of ^{12}CO integrated intensity within $1''$. A local peak in ^{13}CO integrated intensity is also seen within $1''$ of D, E, and G. Each of the four sources also coincides with a local maximum of peak brightness temperature in ^{12}CO and ^{13}CO , and the source D is at the maximum of the C^{18}O brightness temperature map. Though not coincident with an isolated peak, the radio source F is within $1''$ of a ridge of ^{12}CO integrated intensity, and is on a sharp ridge of ^{12}CO peak brightness temperature. In contrast, the sources M2/SSC6 and M3/SSC3 that are thought to be less embedded in dust are indeed in the areas of less molecular gas. The radio sources A and J do not have a nearby peak in the CO maps. Table 4 summarizes the associations of peaks in CO maps to the sources in other wavelengths. In general, the correlation to the sources appears better in peak CO temperature than in the line integrated intensity. The weak 1.3 mm continuum does not coincide with any of the radio and mid-IR sources.

The CO spectra measured at the hotspots are predominantly single-peaked, and the peaks of different isotopic lines are at the same velocity for each hotspot, as shown in Figure 11. This suggests that each hotspot is a single subregion in each gas complex. The properties of CO emission measured at the CO hotspots are summarized in Table 5.

4.5. Seyfert Nucleus

The active nucleus is in the CO deficient area inside the molecular ring, and no CO peak is at the nucleus. The integrated intensity and peak brightness temperature of $^{12}\text{CO}(2-1)$ at the AGN position are $9.3 \text{ Jy km s}^{-1} \text{ arcsec}^{-2}$ and 2.0 K , respectively, in our $2''6 \times 1''8$ resolution data. The surface density of molecular gas in the galaxy plane is $2 \times 10^2 M_{\odot} \text{ pc}^{-2}$ in the central 200 pc for the adopted x_{CO} . The mean total extinction in our line of sight is $\sim 12 \text{ mag}$ (i.e., $N_{\text{H}_2} = 1.2 \times 10^{22} \text{ cm}^{-2}$). The column density and extinction in front of the AGN would be half of these if the nucleus were at the mid-plane of a uniform gas layer. The mass of molecular gas within 100 pc of the nucleus is $6 \times 10^6 M_{\odot}$. The supposed molecular torus confining the conical plasma outflow should be in this region, considering the opening angle of the flow ($\sim 50^\circ$; Hjelm & Lindblad 1996) and the typical scale height of the molecular gas layer ($\lesssim 100 \text{ pc}$) in the centers of disk galaxies. Note that these mass-related quantities inherit the uncertainty of the conversion factor, and that the factor quite possibly changes between the starburst ring and the vicinity of the AGN.

⁹ The radio source H was given positions $1''4$ apart by Sandqvist et al. (1995) and Stevens et al. (1999). We use the average position and associate the source with M8, which is $0''7$ from the radio position. There remains a possibility, however, that there are two radio sources and M7 and M8 are associated with each of them.

We detect no kinematical anomaly at the nucleus, such as high velocity gas suggestive of fast rotation around the AGN or a kinematical sign of a molecular outflow that may be entrained by the plasma outflow. Our spatial resolution, however, is probably insufficient to see gas motion dominated by the central object. The full-width at zero intensity of ^{12}CO line is 270 km s^{-1} at the nucleus. This implies a dynamical mass of $M_{\text{dyn}}(R_g \leq 0.1 \text{ kpc}) \sim 1 \times 10^9 M_{\odot}$ for gas in circular motion in the galaxy plane. This is an order of magnitude larger than the mass of the central engine inferred from the K magnitude of the galaxy by Risaliti et al. (2005). Judging from the PV diagram (Fig. 6), a factor of $\gtrsim 3$ higher resolution is likely needed before one starts to see the gas motion influenced by the expected black hole.

The properties of molecular gas around the AGN can be constrained, though weakly, from the low brightness temperature of ^{12}CO . The physical temperature of molecular gas in the central 200 pc would be 6 K if the gas is uniformly distributed in the region and if ^{12}CO is optically thick and in LTE. Judging from the low temperature, it is more likely that one or more of these conditions is not satisfied; i.e., the gas has clumps, a $^{12}\text{CO}(2-1)$ opacity $\lesssim 1$, subthermal excitation of CO, or a combination of these. The clumpy distribution of the ISM could reduce the extinction toward the AGN, to be more consistent with the optically visible nucleus.

5. BAR-DRIVEN GAS DYNAMICS

The central concentration of molecular gas, with an extent of a few kpc and a mass of $\sim 10^9 M_{\odot}$, is almost an expected feature for NGC 1365 considering the long and prominent bar in the galaxy. A stellar bar is known to drain the gas in the region it sweeps toward the galactic center (e.g., Matsuda & Nelson 1977; Sakamoto et al. 1999b; Sheth et al. 2005). The bar in NGC 1365 has apparently worked as a powerful gas funnel.

The overall distribution of molecular gas in the central concentration can be understood in the framework of the bar-driven gas dynamics, in which the dominant pattern of gas flow changes between the so-called x_1 -type and x_2 -type in the circumnuclear region. The x_1 and x_2 are families of stable, prograde, and periodic orbits for stars in the nonaxisymmetric potential of a galaxy bar (see Binney & Tremaine 1987). The former orbits are elongated along the bar and fill most of it, and the latter, which can exist closer to the galactic center under certain conditions, are elongated perpendicular to the bar. Gas follows similar orbits or streamlines, but because gas is collisional unlike stars the angle between x_1 and x_2 for gas can be oblique and less than 90° measured in the direction of galaxy rotation (Wada 1994). As has been modeled specifically for this galaxy by Teuben et al. (1986) and Lindblad et al. (1996) and for generic barred galaxies by many authors, if there exist x_2 orbits, gas can form a circumnuclear ring or spiral pattern connected to a pair of straighter gas lanes in the bar. What we see in NGC 1365 matches the model gas morphology and what has been seen in many other barred galaxies. The leading-edge gas lanes on the bar are part of the x_1 -like orbits and the gas ring, whose major axis makes an oblique angle less than 90° with the bar, corresponds to the x_2 -like orbits.

Kinematically, there are two pieces of evidence that support the gas dynamical model mentioned above. First, the S shaped isovelocity contours around the systemic velocity ($\S 4.2$) are explicable by the transition of dominant orbits between x_1 -like outside the ring and x_2 -like around the ring as

seen in the models with the x_1 - x_2 transition, or an inner Lindblad resonance (ILR), in Fig. 4 of Teuben et al. (1986) and Fig. 20b of Lindblad et al. (1996). The noncircular motion can be caused purely by the transition (Lindblad & Lindblad 1994), but gas shocks may be also contributing. Secondly, as shown in Fig. 12, the double-peaked line profiles near an apocenter of the circumnuclear ring are consistent with oval gas motion along the ring, whose major axis makes an oblique angle to the bar. This again suggests that x_2 -like gas stream exists on or slightly inside the molecular ring. We note that these kinematical and morphological clues for the presence of a x_1 - x_2 transition are probably more robust than an analysis of the rotation curve by using the resonance condition of $2(\Omega - \Omega_b) = \kappa$, where Ω , Ω_b , and κ are angular frequency, the pattern speed of the bar, and epicyclic frequency, respectively. The resonance condition is known to be a poor indicator for the presence of x_2 orbits in a strong bar (Contopoulos & Papayannopoulos 1980).

6. GAS PROPERTIES

6.1. Average Properties in the Galactic Center

The observed ^{12}CO -to- ^{13}CO intensity ratio, $R_{12/13}^{(2-1)} = 8.7 \pm 2.8$, is normal for the centers of local spiral galaxies including the ones with moderate starburst ($\log(L_{8-1000\ \mu\text{m}}/L_\odot) \lesssim 10.5$). For example, the ratio is about 10 at the centers of our Galaxy, IC342, NGC 253, and M82 (Sawada et al. 2001; Meier et al. 2000; Mao et al. 2000; Sakamoto et al. 2006a). The ratio separates NGC 1365 from the more infrared luminous mergers ($\log(L_{8-1000\ \mu\text{m}}/L_\odot) \gtrsim 11.5$), which are known to show higher ratios of $R_{12/13}^{(2-1)} \gtrsim 20$ (Casoli et al. 1992; Aalto et al. 1995; Glenn & Hunter 2001; Sakamoto et al. 2006b).

There are three basic circumstances under which the ^{12}CO -to- ^{13}CO intensity ratio is about 10, although some of their intermediate situations also produce the same ratio. The three correspond to the three parts of the formal expression of the ratio:

$$R_{12/13} = \frac{(1 - e^{-\tau_{12}}) [J(T_{\text{ex},12}) - J(T_{\text{CMB}})] f_{\text{b},12}}{(1 - e^{-\tau_{13}}) [J(T_{\text{ex},13}) - J(T_{\text{CMB}})] f_{\text{b},13}},$$

where τ , T_{ex} , and f_{b} are optical depth, excitation temperature, and beam filling factor, respectively, and $J(T)$ is the effective radiation temperature $(h\nu/k)/[\exp(h\nu/kT) - 1]$ for the line frequency denoted as ν . First, if the CO is thermalized at least up to the J=2 level and if the two isotopic lines have almost the same beam-filling factors, then the ratio is determined by the optical depths. For example, the ratio of 8.7 corresponds to $\tau_{^{13}\text{CO}(2-1)} = 0.12$ and ^{13}CO column density of $5 \times 10^{15} \text{ cm}^{-2} (\text{km s}^{-1})^{-1}$ for a 50 K gas in LTE. The molecular gas needs to be turbulent, with a characteristic velocity gradient of $dv/dr \sim 15 \text{ km s}^{-1} \text{ pc}^{-1}$, to have a hydrogen density exceeding $n_{\text{H}_2} \sim 10^4 \text{ cm}^{-3}$ to maintain the excitation. Secondly, the ratio of ~ 10 can also be observed when the ^{13}CO excitation is highly subthermal. In the non-LTE analysis using the large velocity gradient model (Goldreich & Kwan 1974), the mean ratio of 8.7 requires a gas density of $n_{\text{H}_2} \sim 3 \times 10^2 \text{ cm}^{-3}$ for the abundances of $[\text{H}_2/^{12}\text{CO}] = 10^4$ and $[^{12}\text{CO}/^{13}\text{CO}] = 40$ and a velocity gradient in clouds of $1 \text{ km s}^{-1} \text{ pc}^{-1}$. Gas temperatures in the range of 10 – 300 K produce the same result. In these conditions, the excitation to J=2 is subthermal with ^{13}CO having lower excitation temperature than ^{12}CO , and the $^{13}\text{CO}(2-1)$ opacity is 0.5–0.9. Finally, different beam filling factors of the two lines can affect the ratio if molecular clouds

in the galactic center have a core-envelope structure as has been observed in the Galactic center and suggested in luminous mergers (Hüttemeister et al. 1995; Aalto et al. 1995). In this case, ^{12}CO traces lower density envelopes while ^{13}CO is emitted from higher density cores.

Our mass estimate of molecular gas assumes the nearly thermalized excitation of the first case rather than the very subthermal one in the second. In the latter, $\text{C}^{18}\text{O}(2-1)$ excitation temperature is about a tenth of the thermal gas temperature for a 50 K gas. Even though we already allowed for the contribution of thin gas, our mass estimates would need to be doubled if most of the C^{18}O and ^{13}CO emission is from very poorly excited molecules. Large turbulence in molecular gas, which separates the thermalized case from the subthermal one, has been suggested to be a characteristic feature of the Galactic center (Sawada et al. 2001). The turbulence is measured with a velocity gradient in the escape probability approximation and is larger than $10 \text{ km s}^{-1} \text{ pc}^{-1}$. We expect the starburst nucleus of NGC 1365 has no less turbulence than the Galactic center, and hence keep our mass estimates. The very low excitation of C^{18}O and ^{13}CO can not be ruled out, however, without further observations.

6.2. Spatial Variation

The variation of $R_{12/13}^{(2-1)}$ within the circumnuclear region, by about a factor of 3 at our resolution, allows multiple interpretations corresponding to the three cases mentioned above. In the thermalized case, a factor of 3 lower ratio can mean a gas column density per velocity (N_{H_2}/dv) increased by the same factor, or a gas temperature reduced by about a factor of 2. In the subthermal case, a higher gas density reduces the ratio. In the filling-factor model, molecular clouds in lower $R_{12/13}$ regions have smaller envelopes with respect to their cores.

Our data show the lack of an organized pattern in the $R_{12/13}^{(2-1)}$ ratio, except for the slight difference between the near and far sides. This makes it difficult to assess the gas properties by combining the line ratio and other information. For example, it is possible that molecular gas is relatively dense in the twin peaks owing to the convergence of gas flow (Ott et al. 2005). One of them, the gas complex containing radio sources D, E, and G, shows a lower ratio of ~ 8 than other bright ^{12}CO complexes, which have ratios $\gtrsim 10$ (Fig. 8). This is consistent with the higher density, which also makes N_{H_2}/dv higher for a constant turbulence (dv/dr). However, there are regions having even lower ratios without obvious dynamical reasons. Quite possibly, multiple parameters change at the same time for multiple reasons, making any large-scale ratio pattern less clear.

On smaller scales, our data also show no distinctive correlation between $R_{12/13}^{(2-1)}$ and the radio, optical, and IR sources. This likely means that the effect of these sources on the surrounding molecular gas is either small in terms of the ratio or is heavily diluted in our 200 pc beam. The former is possible, for example, if higher gas temperature around a cluster, which could reduce the optical depths of the CO lines for a constant column density, is offset by the gas concentration (i.e., larger column density) around the clusters. The ratio $R_{12/13}$, which traces the ^{13}CO optical depth in the thermalized case, would then be comparable toward the clusters and the surrounding area. Finally, it is noteworthy that the high ratio of ≥ 20 observed in luminous mergers in kpc beams is not observed in any part of the starburst region.

7. CIRCUMNUCLEAR STAR FORMATION

7.1. Star Formation Law

The circumnuclear starburst in NGC 1365 follows the two empirical scaling relations of Kennicutt (1998, hereafter K98) for starburst galaxies. Taking 1 kpc as the radius of the starburst region, and attributing half of the far-IR luminosity of the galaxy to the starburst (see §2), the star formation rate in the region is $9 M_{\odot} \text{ yr}^{-1}$ and its surface density is $\Sigma_{\text{SFR}} = 3 M_{\odot} \text{ yr}^{-1} \text{ kpc}^{-2}$ for the star formation rate-to-far-IR luminosity relation of K98. The mean surface density of H_2 in the region is $\Sigma_{\text{H}_2} = 1 \times 10^3 (x_{\text{CO}}/2.8) M_{\odot} \text{ pc}^{-2}$; K98 adopted $x_{\text{CO}} = 2.8$. Fig. 13 shows that NGC 1365 with these surface densities follows the correlation, or the Schmidt law, seen among circumnuclear starbursts. The galaxy also follows the same correlation for a combined sample of starbursts and normal galaxy disks (see Fig. 6 in K98). In addition, NGC 1365 follows another correlation between gas surface density normalized by the dynamical time and the star formation surface density. The former is $\Sigma_{\text{H}_2}/T_{\text{dyn}} = 4 \times 10^1 (x_{\text{CO}}/2.8) M_{\odot} \text{ yr}^{-1} \text{ kpc}^{-2}$ for the starburst region having the T_{dyn} calculated in §4.2. This and the abovementioned Σ_{SFR} place NGC 1365 on the tight correlation between the two quantities seen in Fig. 7 of K98, with the abscissa and ordinate being 3.6 and 0.5, respectively, in the figure's units.

The fact that the circumnuclear starburst in NGC 1365 follows these empirical correlations is not affected by the choice of the conversion relations used to derive H_2 mass and star formation rate, because we use the same conversion factors as in K98. Removing the conversion relations and stated in observed quantities, the circumnuclear starburst in the central 2 kpc of NGC 1365 follows the correlation, seen among starbursts and galactic disks, between far-IR luminosity averaged over the star forming region and CO (J=1–0 equivalent) luminosity averaged in the same area. The second correlation that NGC 1365 follows can be also stated only using observed quantities. The factor of ~ 6 difference in the CO to H_2 conversion factor between this paper and K98 only affects such quantities as gas consumption time and gas-to-dynamical mass ratio. The time in which the current amount of gas would be consumed by the star formation at the current rate is $1 \times 10^8 \text{ yr}$ in the 2 kpc-diameter starburst region for the conversion factor we adopted, and it is 6 times longer for the disk X_{CO} used in K98. Note that Kennicutt (1998) used the disk conversion factor for his sample only for the sake of simplicity, being fully aware that the factor can change in starburst environment.

7.2. Reasons for the Large Luminosity

The reasons for the starburst in NGC 1365 being one of the most luminous in non-merging galaxies while following the normal star formation laws are the high gas surface density in the starburst and the large size of the starburst region. The mean gas surface density in the starburst is among the highest observed in non-merging starburst galaxies, as seen in Fig. 13 where the galaxy has the fourth highest Σ_{H_2} , only after NGC 3079, M82, and NGC 253, among 17 non-merging starbursts. The central gas-surface density of NGC 1365 also stands out when compared to those in the NRO–OVRO survey of nearby galaxies (Sakamoto et al. 1999a,b). The high-resolution survey gives gas surface densities in the central kiloparsec of 20 spirals, including some starbursts but no merger. The gas surface density in the central kpc of NGC 1365 is $\Sigma_{\text{mol}}(R_g \leq 500 \text{ pc}) = 4 \times 10^2 (x_{\text{CO}}/0.5) M_{\odot} \text{ pc}^{-2}$ and

is twice larger than the largest in the survey if the same x_{CO} is used for all galaxies. Meanwhile, the extent of the circumnuclear starburst in NGC 1365, $\sim 2 \text{ kpc}$, is among the largest compared to those in K98 and surveys by Jogee et al. (2005, Fig. 5) and Knapen et al. (2006, Fig. 1). Obviously, the high gas surface density in the large area needs a large amount of gas; $M_{\text{mol}}(r_g < 1 \text{ kpc}) \sim 10^9 M_{\odot}$ (§4.1). For this accumulation, the large size of the galaxy ($L_B \approx 6 \times 10^{10} L_{\odot} \approx 3L_B^*$, $D_{25} = 59 \text{ kpc}$; de Vaucouleurs et al. 1991) and the long bar ($l_{\text{bar}} \sim 18 \text{ kpc}$) were probably crucial through the bar-driven transport of disk gas. Thus the combination could be regarded as a deeper cause for the luminous starburst.

The luminous starburst in NGC 1365 contains subregions comparable to the entire starbursts in M82 and NGC 253. Most notably, the northeastern edge of the circumnuclear ring has $\Sigma_{\text{H}_2} \approx 3 \times 10^3 (x_{\text{CO}}/2.8) M_{\odot} \text{ pc}^{-2}$, or the same gas surface density as in those two starbursts for the same extent of $\sim 400 \text{ pc}$ and for the same x_{CO} . The radio and mid-IR sources in the region suggest enhanced Σ_{SFR} there. With a few such subregions, it is reasonable that NGC 1365's starburst is a factor of 2–4 more luminous than those in M82 and NGC 253. Although the empirical star formation laws in the previous section and the scaling observation like this leave out the physics of star formation on smaller scales, they are still useful to obtain an overview — star formation in this luminous starburst is not discrete in nature from those in less luminous starbursts.

It remains to be found out why the luminous starburst is seen *now* even though it can last only for $\sim 10^8 \text{ yr}$. Roy & Walsh (1997) suggested that the bar was young (age $\sim 1 \text{ Gyr}$) and started the gas transport in the recent past on the basis of a bend in the radial gradient of O/H abundance, but the existence of the bend has been disputed by Pilyugin (2003). The galaxy is a member of the Fornax cluster, but lacks an obvious interacting partner for strong gravitational disturbance. H I imaging by Jörsäter & van Moorsel (1995) does not reveal a sign of recent galaxy interaction either, though the outer H I disk shows a hint of interaction with the intergalactic medium. It may be that the starburst has been turning on and off without external triggers, perhaps owing to a threshold in the star formation mechanism (Jogee et al. 2005). If so, the star formation law must switch between the one for the starburst state (e.g., Fig. 13) and the other for non-starburst.

7.3. CO Hotspots and Super Clusters

We saw in §4.4 that the molecular ring contains several CO hotspots and that three of them are spatially associated with the radio/mid-IR sources D/M4, E/M5, and G/M6 that are suggested to be super clusters of $\sim 10^6 M_{\odot}$, $\sim 10^9 L_{\odot}$ and ages of 3–6 Myr by Galliano et al. (2005). Another source, H/M8, also coincides with a CO hotspot, but it is fainter and does not have age and mass estimates. It is possible that each of the radio/mid-IR sources is a group of clusters rather than a single cluster, since their sizes are only constrained to be $\leq 20\text{--}60 \text{ pc}$ (Sandqvist et al. 1995; Galliano et al. 2005) while super clusters have sizes of $\lesssim 10 \text{ pc}$. We refer each source as a super cluster for simplicity, but 'a cluster' in the following can be 'a cluster complex'.

The empirical star formation laws that we found applicable to the circumnuclear region as a whole allow the amount of star formation needed for the clusters. A star formation rate of $\Sigma_{\text{SFR}} \approx 20 M_{\odot} \text{ yr}^{-1} \text{ kpc}^{-2}$ is expected from the star formation laws in K98 for the typical CO integrated intensity on the circumnuclear ring, $I_{\text{CO}2-1} \approx 150 \text{ Jy km s}^{-1}$

beam⁻¹ equivalent to an inclination corrected surface density of $\Sigma_{\text{H}_2} \approx 3 \times 10^3 (x_{\text{CO}}/2.8) M_{\odot} \text{pc}^{-2}$. Thus, if the star formation laws apply to 100 pc scales, $10^6 M_{\odot}$ of stars will form every 5 Myr in every 100 pc by 100 pc area in the molecular ring. The empirical laws, however, do not tell whether and where a compact and massive cluster forms. The spatial association of the putative $\sim 10^6 M_{\odot}$ clusters and the CO hotspots may be a valuable observational clue to address these points.

The significance of the hotspot-cluster association is that the CO hotspots were very likely the sites of cluster formation in the recent past for two reasons. First, the clusters' relative motion with respect to the ambient gas in their ~ 5 Myr lives would be $\lesssim 50$ pc if we assume the clusters' relative velocities against the ambient gas to be $\sim 10 \text{ km s}^{-1}$, which is a typical velocity dispersion of molecular clouds in galaxies. According to this estimate, the CO hotspots seen in our ~ 200 pc resolution images are composed of gas that was in the immediate vicinity of the formation sites of the super clusters. Second, given the non-trivial configuration of the three hotspot-cluster pairs, it is unlikely that the three clusters formed elsewhere and have migrated to the CO hotspots, unless the clusters themselves affected their ambient gas to create the hotspots. This argument reinforces the first one, in which the drift velocity might be larger than assumed because the three clusters are in the region with two types of orbits and because only gas is subject to hydrodynamical forces. Regarding the possibility that the clusters caused the hotspots rather than the gas hotspots formed the clusters, we favor the latter interpretation though our data do not rule out the former. Our preference is because three hotspots are visible in ^{13}CO and one even in C^{18}O . Elevation of gas temperature, the most likely effect of a young cluster on its ambient gas, does not increase the intensity of an optically thin CO line per unit mass of molecular gas if the isotope CO is well excited, which we favorably discussed in §6.1.

In our more favored model, the CO hotspots are peaks of gas surface density. The surface density is either that for the entire velocity or for a 10 or 20 km s^{-1} range depending on whether the hotspot is in the integrated map or in the peak temperature map. Gas temperature can also be higher in the hotspots seen in ^{12}CO because the brightness temperature of the line is the gas temperature multiplied by the beam filling factor. The gas surface densities in the hotspots are $\Sigma_{\text{mol}} \sim 10^3 M_{\odot} \text{pc}^{-2}$ when averaged over 200 pc scale (see Fig. 5). The CO hotspot-cluster associations suggest that the super clusters formed in such a high surface-density environment. If the high surface density of molecular gas is one of the requirements for the SSC formation, then SSC formation predominantly in starbursts can be a consequence of the high gas surface densities in starburst regions.

In the alternative interpretation, the CO hotspots are largely due to higher gas temperature there, plausibly owing to the luminous super clusters. For optically thick ^{12}CO , this straightforwardly explains the hotspots. For ^{13}CO and C^{18}O , this interpretation is possible only when the gas excitation is sub-thermal and the isotope lines have moderate (~ 1) optical depths as in the second case in §6.1. In such a situation, a higher gas temperature can increase the excitation temperature of the subthermally-excited CO without significantly reducing the line optical depth, and hence can increase the line brightness temperature. The gas surface densities at the hotspots in this case would be higher than in the thermalized case (§6.1), even though the hotspots may not be local peaks

of gas surface density.

7.3.1. Similar Sources in Other Galaxies

There have been a small number of cases, in other galaxies, that are similar to the CO hotspot-cluster associations. Table 6 compares them with those in NGC 1365. These cases show that at least some of the most massive and youngest clusters in starbursts are accompanied by CO hotspots detectable at ~ 100 pc resolutions.

One case is in the Antennae merger (NGC 4038/4039). The brightest 15 μm source in the system, located in the overlap region of the colliding galaxies, is associated with a molecular complex called SGM4–5 (Wilson et al. 2000; Mirabel et al. 1998). Their parameters are within a factor of a few from those of the CO hotspot-cluster associations in NGC 1365 considering the larger CO beam and hence more beam dilution in the Antennae. The source has been suggested to be a young (~ 4 Myr), massive ($\sim 10^7 M_{\odot}$), and compact ($R_{\text{half light}} \sim 30$ pc) cluster or cluster complex with thousands of O stars and a total luminosity of $\sim 10^9 L_{\odot}$ (Gilbert et al. 2000; Neff & Ulvestad 2000; Haas et al. 2000). Since the cluster is in the molecular complex but not at its CO peak, the CO hotspot is most likely a peak of gas surface density. Statistically, Zhang et al. (2001) showed that young clusters (of ages ~ 5 Myr, including the one mentioned above) in this galaxy are better associated with mid/far-IR, CO, and radio sources than older clusters.

Another case is in the barred starburst spiral M83. The brightest CO peak in the galaxy's circumnuclear region, in both integrated intensity and brightness temperature, coincides with a radio and mid-IR peak (Sakamoto et al. 2004; Turner & Ho 1994; Telesco et al. 1993). The radio and mid-IR emission is due to star formation, though there may be contribution from a radio supernova to the radio peak (Turner & Ho 1994; Telesco et al. 1993). The CO hotspot is on a circumnuclear gas ring and is where x_1 -like and x_2 -like gas streamlines converge. The hotspot location with respect to the bar and the circumnuclear gas ring is therefore identical to that in NGC 1365.

7.4. Cluster and Hotspot Evolution

It has been proposed that gravitational collapse in an ILR gas ring, where a bar accumulates disk gas, forms gas clumps and subsequently causes intense star formation in them (Wada & Habe 1992; Elmegreen 1994). The CO hotspots with embedded young super clusters may be such gas clumps. If the molecular hotspots are high surface-density regions of molecular gas, possibly caused by gravitational instability, then the formation of super clusters from such giant gas concentrations of ~ 100 pc and $> 10^7 M_{\odot}$ scales is in accordance with the supergiant-cloud model for the formation of super clusters (Wilson et al. 2003, and references therein). The CO hotspot-cluster association, however, is also compatible with another model for SSC formation where a super cluster forms from a moderate-size molecular cloud ($\lesssim 10^6 M_{\odot}$) by converting most of the gas into stars (Keto et al. 2005, and references therein). Such clouds quite possibly exist in the high surface-density environment of the CO hotspots and could have had such triggers as cloud collision and compression by nearby H II regions or supernova remnants. High surface-density clouds with a few 10 pc sizes and velocity widths of the order of 10 km s^{-1} could cause the CO hotspots in the peak temperature maps.

The SSCs in the hotspots are expected to disperse ambient gas as they age while blowing stellar winds and having supernovae. A super cluster may cause an expanding bubble or even an outflow of the ISM from the disk (e.g., Sakamoto et al. 2006a,b, in our SMA survey). Such features may quite possibly be hidden within the CO hotspots. The optically-visible super clusters that are not associated with CO hotspots, most notably M2/SSC6 and M3/SSC3, may be older super clusters that have already dispelled their dust cocoons in which they formed. Alternatively, they could have formed from isolated molecular clouds and have mostly consumed them at the time of formation.

8. SUMMARY

We have observed 1.3 mm CO lines and continuum in the center of the barred spiral galaxy NGC 1365 at high spatial resolutions. The circumnuclear starburst in the galaxy is among the most luminous and intense in non-merging galaxies. Our main findings regarding the properties of molecular gas and their relation to the starburst and to the Seyfert nucleus are as follows.

1. There is an oval ring of molecular gas around the nucleus, having a ~ 2 kpc extent and twin-peak enhancements at its apocenters, and connected to gas lanes on the leading side of the stellar bar. The gas morphology and kinematics in the region are consistent with the model that the ring is at the transition region between x_1 - and x_2 -like gas streamlines in the bar. The structure is typical of barred galaxies.
2. The molecular ring coincides with the starburst ring seen in radio emission, suggesting that the gas distribution largely determines the extent and the shape of the starburst. Moreover, the intensity of the starburst averaged over the circumnuclear region is what is expected from the molecular gas surface density of the region and the star formation laws in Kennicutt (1998). A plausible synopsis of the galaxy's starburst is as follows: The long (~ 18 kpc) stellar bar funneled a large amount of molecular gas ($\sim 10^9 M_\odot$) toward the galactic center, and the resulting high gas surface density ($\sim 10^3 M_\odot \text{ pc}^{-2}$) in the relatively large circumnuclear ring ($r \sim 1$ kpc) resulted in the starburst ($\sim 3 M_\odot \text{ yr}^{-1} \text{ kpc}^{-2}$) of large total luminosity ($\sim 10^{11} L_\odot$) following the star formation laws. — A remaining question is why the transient starburst (gas consumption timescale $\sim 10^8 \text{ yr}$) is seen now.
3. There are compact ($\lesssim 200 \text{ pc}$) peaks of CO integrated intensity and brightness temperature, which we call CO hotspots, on the circumnuclear ring. Some of the hotspots coincide with the radio and mid-IR sources that have been identified as dust-enshrouded super star clusters. The association of the CO hotspots and super clusters allows two interpretations. The first one is that the most luminous and presumably massive super clusters were formed in regions with the highest gas surface densities ($\sim 10^3 M_\odot \text{ pc}^{-2}$ in 200 pc scale). The second one is that the luminous embedded clusters heated their ambient gas to form the hotspot. The former, which is more conventional in terms of the interpretation of CO intensities at $\gtrsim 100 \text{ pc}$ scales, implies a relation between the cluster formation and gas complexes already identifiable at a 200 pc resolution.

4. The active nucleus coincides with the dynamical center of the galaxy within 30 pc, according to the CO velocity field. Neither integrated intensity nor brightness temperature of CO peaks at the nucleus. We found no anomaly in molecular gas that may be related to the AGN.

We thank the SMA staff for their help prior to and during our observations, Jun-Ichi Morino and Andrew Baker for stimulating discussions, Raffaella Morganti for kindly providing her radio data, and the anonymous referee for his/her helpful comments. This research made use of NED, ADS, and the HST archive, in addition to the SMA; we are grateful to their operating, funding, and contributing people and agencies.

Facilities: SMA, HST (WFPC2)

REFERENCES

- Aalto, S., Booth, R. S., Black, J. H., and Johansson, L. E. B. 1995, *A&A*, 300, 369
- Barth, A. J., Ho, L. C., Filippenko, A. V., and Sargent, W. L. 1995, *AJ*, 110, 1009
- Binney, J. and Tremaine, S. 1987, *Galactic Dynamics*, (Princeton: Princeton Univ. Press)
- Bridle, A. H., and Greisen, E. W. 1994, *NRAO AIPS Memo* 87
- Bryant, P. M., and Scoville, N. Z. 1996, *ApJ*, 457, 678
- Casoli, F., Dupraz, C., and Combes, F. 1992, *A&A*, 264, 55
- Contopoulos, G., Papayannopoulos, T. 1980, *A&A*, 90, 33
- Curran, S. J., Polatidis, A. G., Aalto, S., and Booth, R. S. 2001, *A&A*, 368, 824
- Dahmen, G., Hüttemeister, S., Wilson, T. L., and Mauersberger, R. 1998, *A&A*, 331, 959
- Dame, T. M., Hartmann, D., and Thaddeus, P. 2001, *ApJ*, 547, 792
- de Grijp, M. H. K., Miley, G. K., Lub, J., and de Jong, T. 1985, *Nature*, 314, 240
- de Vaucouleurs, G., de Vaucouleurs, A., Corwin, H. G., Buta, R. J., Paturel, G., & Fouque, P. 1991, "Third Reference Catalogue of Bright Galaxies", (Springer Verlag)
- Elmegreen, B. G. 1994, *ApJ*, 425, L73
- Forbes, D. A., Norris, R. P. 1998, *MNRAS*, 300, 757
- Freedman, W. L., et al. 2001, *ApJ*, 553, 47
- Galliano, E., Alloin, D., Pantin, E., Lagage, P. O., and Marco, O. 2005, *A&A*, 438, 803
- Gilbert, A. M. et al. 2000, *ApJ*, 533, L57
- Glenn, J., and Hunter, T. R. 2001, *ApJS*, 135, 177
- Goldreich, P. & Kwan, J. 1974, *ApJ*, 189, 441
- Haas, M., Klaas, U., Coulson, I., Thommes, E., and Xu, C. 2000, *A&A*, 356, L83
- Henkel, C., and Mauersberger, R. 1993, *A&A*, 274, 730
- Hjelm, M., and Lindblad, P. O. 1996, *A&A*, 305, 727
- Ho, P. T. P., Moran, J. M., Lo, K. Y. 2004, *ApJ*, 616, L1
- Hunter, S. D., et al. 1997, *ApJ*, 481, 205
- Hüttemeister, S., Wilson, T. L., Mauersberger, R., Lemme, C., Dahmen, G., and Henkel, C. 1995, *A&A*, 294, 667
- Iyomoto, N., Makishima, K., Fukazawa, Y., Tashiro, M., and Ishisaki, Y. 1997, *PASJ*, 49, 425
- Jarrett, T. H., Chester, T., Cutri, R., Schenfelder, S. E., and Huchra, J. P. 2003, *AJ*, 125, 525
- Jogee, S., Scoville, N., and Kenney, J. D. P. 2005, *ApJ*, 630, 837
- Jörsäter, S. and van Moorsel, G. A. 1995, *AJ*, 110, 2037
- Kenney, J. D. P., Wilson, C. D., Scoville, N. Z., Devereux, N. A., and Young, J. S. 1992, *ApJ*, 395, L79
- Kennicutt, R. C. 1998, *ApJ*, 498, 541 (K98)
- Keto, E., Ho, L. C., and Lo, K. -Y. 2005, *ApJ*, 635, 1063
- Knapen, J. H., Mazzuca, L. M., Böker, T., Shlosman, I., Colina, L., Combes, F., and Axon, D. J. 2006, *A&A*, 448, 489
- Komossa, S. and Schulz, H. 1998, *A&A*, 339, 345
- Kristen, H., Jorsater, S., Lindblad, P. O., and Bokserberg, A. 1997, *A&A*, 328, 483
- Kronberg, P. P., Biermann, P., and Schwab, F. R. 1985, *ApJ*, 291, 693
- Lindblad, P. A. B., Lindblad, P. O., and Athanassoula, E. 1996, *A&A*, 313, 65
- Lindblad, P. O., and Lindblad, P. A. B. 1994, *ASP Conf. Ser.* 66: *Physics of the Gaseous and Stellar Disks of the Galaxy*, 66, 29
- Lindblad, P. O., 1999, *A&AS*, 9, 221
- Maloney, P., and Black J. H. 1988, *ApJ*, 325, 389
- Mao, R. Q. et al. 2000, *A&A*, 358, 433
- Matsuda, T., and Nelson, A. H. 1977, *Nature*, 266, 607
- Matsushita, S., Saito, M., Sakamoto, K., Hunter, T.R., Patel, N.A., Sridharan, T.K., and Wilson, R.W. 2006, *Proc. SPIE*, 6275, 62751W
- Meier, D. S., Turner, J. L., and Hurt, J. L. 2000, *ApJ*, 531, 200
- Meier, D. S., and Turner, J. L. 2001, *ApJ*, 551, 687
- Meier, D. S., and Turner, J. L. 2004, *AJ*, 127, 2069
- Miley, G. K., Neugebauer, G., and Soifer, B. T. 1985, *ApJ*, 293, L11
- Mirabel, I. F. et al. 1998, *A&A*, 333, L1
- Morgan, W. W. 1958, *PASP*, 70, 364
- Morganti, R., Tsvetanov, Z. I., Gallimore, J., and Allen, M. G. 1999, *A&AS*, 137, 457
- Neff, S. G., and Ulvestad, J. S. 2000, *AJ*, 120, 670
- Oka, T., Hasegawa, T., Hayashi, M., Handa, T., and Sakamoto, S. 1998, *ApJ*, 493, 730
- Ott, J., Weiß, A., Henkel, C., and Walter, F. 2005, in *AIP Conf. Proc.* 783, *The Evolution of Starbursts*, ed. S. Hüttemeister et al., 141
- Papadopoulos, P. P., and Seaquist, E. R. 1998, *ApJ*, 492, 521
- Phillips, M. M., Turtle, A. J., Edmunds, M. G., and Pagel, B. E. J. 1983, *MNRAS*, 203, 759
- Pilyugin, L. S. 2003, *A&A*, 397, 109
- Regan, M., and Elmegreen, D. M. 1997, *AJ*, 114, 965
- Risaliti, G., Elvis, M., Fabbiano, G., Baldi, A., and Zezas, A. 2005, *ApJ*, 623, 93
- Roussel, H., et al. 2001, *A&A*, 372, 406
- Roy, J. -R., and Walsh, J. R.
- Saikia, D. J., Pedler, A., Unger, S. W., and Axon, D. J. 1994, *MNRAS*, 270, 46
- Sakamoto, K., Okumura, S. K., Ishizuki, S., and Scoville, N. Z. 1999a, *ApJS*, 124, 403
- Sakamoto, K., Okumura, S. K., Ishizuki, S., and Scoville, N. Z. 1999b, *ApJ*, 525, 691
- Sakamoto, K., Matsushita, S., Peck, A. B., Wiedner, M. C., and Iono, D. 2004, *ApJ*, 616, L59
- Sakamoto, K. et al. 2006a, *ApJ*, 636, 685
- Sakamoto, K., Ho, P. T. P., and Peck, A. B. 2006b, *ApJ*, 644, 862
- Sanders, D. B., Solomon, P. M., and Scoville, N. Z. 1984, *ApJ*, 276, 182
- Sanders, D. B., Mazzarella, J. M., Kim D. -C., Surace, J. A., and Soifer, B. T. 2003, *AJ*, 126, 1670
- Sandqvist, A., Jörsäter, S., and Lindblad, P. O. 1982, *A&A*, 110, 336
- Sandqvist, A., Elfhang, T., and Jörsäter, S. 1988, *A&A*, 201, 223
- Sandqvist, A., Jörsäter, S., and Lindblad, P. O. 1995, *A&A*, 295, 585
- Sandqvist, A. 1999, *A&A*, 343, 367
- Sault, R. J., Teuben P. J., and Wright M. C. H. 1995, in *ASP Conf. Ser.* 77, *Astronomical Data Analysis Software and Systems IV*, ed. R. Shaw et al. (San Francisco: ASP), 433
- Sawada, T. et al. 2001, *ApJS*, 136, 189
- Scoville, N. Z., Carlstrom, J. E., Chandler, C. J., Phillips, J. A., Scott, S. L., Tilanus, R. P. J., and Wang, Z. 1993, *PASP*, 105, 1482
- Sérsic, J. L., and Pastoriza, M. 1967, *PASP*, 79, 152
- Sheth, K., Vogel, S. N., Regan, M. W., Thornley, M. D., and Teuben, P. J. 2005, *ApJ*, 632, 217
- Sodroski, T. J. et al. 1995, *ApJ*, 452, 262
- Stevens, I. R., Forbes, D. A., and Norris, R. P. 1999, *MNRAS*, 306, 479
- Strong, A. W., Moskalenko, I. V., Reimer, O., Digel, S., and Diehl, R. 2004, *A&A*, 422, L47
- Stutzki, J., and Güsten, R. 1990, *ApJ*, 356, 513
- Telesco, C. M., Dressel, L. L., and Wolstencroft, R. D. 1993, *ApJ*, 414, 120
- Teuben, P. J., Sanders, R. H., Atherton, P. D., and van Albada, G. D. 1986, *MNRAS*, 221, 1
- Thean, A., Pedlar, A., Kukula, M. J., Baum, S. A., O'Dea, C. P. 2000, *MNRAS*, 314, 573
- Thim, F., Tammann, G. A., Saha, A., Dolphin, A., Sandage, A., Tolstoy, E., and Lbhardt, L. 2003, *ApJ*, 590, 256
- Turner, J. L., and Ho, P. T. P. 1994, *ApJ*, 421, 122
- Ulvestad, J. S., and Antonucci, R. R. J. 1997, *ApJ*, 488, 621
- Veilleux, S., Shopbell, P. L., Rupke, D. S., Bland-Hawthorn, J., and Cecil, G. 2003, *AJ*, 126, 2185
- Wada, K. 1994, *PASJ*, 46, 165
- Wada, K., & Habe, A. 1992, *MNRAS*, 258, 82
- Weiler, K. W., Panagia, N., Montes, M. J., and Sramek, R. A. 2002, *ARA&A*, 40, 387
- Whitmore, B. C., and Schweizer, F. 1995, *AJ*, 109, 960
- Wild, W., et al. 1992, *A&A*, 265, 447
- Wilson, C. D., Scoville, N. Z., Madden, S. C., and Charmandaris, V. 2000, *ApJ*, 542, 120
- Wilson, C. D., Scoville, N. Z., Madden, S. C., and Charmandaris, V. 2003, *ApJ*, 599, 1049
- Wilson, T. L., and Rood, R. 1994, *ARA&A*, 32, 191
- Zhang, Q., Fall, S. M., and Whitmore, B. C. 2001, *ApJ*, 561, 727

TABLE 1
NGC 1365 PARAMETERS

parameter	value	ref.
distance [Mpc]	17.95	1
scale	1''=86 pc, 11''=5 kpc	
inclination [deg.]	40	2
major axis P.A. [deg.]	220	2
bar P.A. [deg.]	90	3,4,5
nucleus ^a R.A. (J2000)	03 ^h 33 ^m 36 ^s .38	5,6,7
Dec. (J2000)	-36°08'25''.7	5,6,7
$\log(L_{8-1000 \mu\text{m}}/L_{\odot})$	11.00	8
Hubble type	SB(s)b	9

REFERENCES. — 1. Freedman et al. (2001); 2. Jörsäter & van Moorsel (1995); 3. Lindblad et al. (1996); 4. Regan & Elmegreen (1997); 5. Measured in the data of Jarrett et al. (2003); 6. Sandqvist et al. (1982); 7. Stevens et al. (1999); 8. Sanders et al. (2003); 9. de Vaucouleurs et al. (1991)

^aThe adopted mean position is within 0''45 of the positions in three wavelengths.

TABLE 2
SMA OBSERVATION PARAMETERS

parameter	value	
date (UT)	2003-12-23	2004-02-02
array configuration	compact	extended
No. of antennas	6	7
τ_{225} ^a	0.08	0.05
$\langle T_{\text{sys}}(\text{DSB}) \rangle^{\text{b}}$ [K]	210	160
$S_{\nu}(\text{J0132-169})^{\text{c}}$ [Jy]	1.38/1.35	1.28/1.20
$S_{\nu}(\text{J0457-234})^{\text{c}}$ [Jy]	1.28/1.20	0.77/0.75
baseline length [m]	6.8–64.9	11.4–175.0
integration time ^d [hr]	3.8	2.7
center frequency, L/U [GHz]	218.600/228.600	
bandwidth [GHz]	2.0	
spectral resolution [MHz]	0.8125	
mosaic center (J2000)	$\alpha=$ 03 ^h 33 ^m 36 ^s .40 $\delta=-$ 36°08'25''.7	
primary beam ^e [arcsec]	54/52	
mosaic field of view [arcsec ²]	100 × 50	
rms noise ^f [mJy beam ⁻¹]	67, 28, 37, 4	

^aZenith opacity at 225 GHz measured at the Caltech Submillimeter Observatory next to the SMA.

^bMedian system temperature toward NGC 1365.

^cFlux density of the calibrator. LSB/USB.

^dIntegration time on the galaxy.

^eThe full width at half maximum of the primary beam approximated to be a circular Gaussian. LSB/USB.

^fNoise in the ¹²CO, ¹³CO, C¹⁸O cubes and in the continuum data, respectively, used for Fig. 2. Those for line data are the ones in each channel. The velocity resolution is 10 km s⁻¹ for ¹²CO and 20 km s⁻¹ for other lines.

TABLE 3
MEASURED AND DERIVED PARAMETERS

parameter	value	unit
$S_{12\text{CO}(2-1)}(R_g \leq 1 \text{ kpc})$	4.3×10^3	Jy km s^{-1}
$S_{13\text{CO}(2-1)}(R_g \leq 1 \text{ kpc})$	3.8×10^2	Jy km s^{-1}
$S_{\text{C}^{18}\text{O}(2-1)}(R_g \leq 1 \text{ kpc})$	1.1×10^2	Jy km s^{-1}
$\max I_{12\text{CO}(2-1)}$	42	$\text{Jy km s}^{-1} \text{ arcsec}^{-2}$
$\max T_{\text{b}, 12\text{CO}(2-1)}$	13	K
$M_{\text{mol}}(R_g \leq 1 \text{ kpc})$	9×10^8	M_{\odot}
$\max \Sigma_{\text{mol}}$	9×10^2	$M_{\odot} \text{ pc}^{-2}$
V_{sys} (radio, LSR)	1618	km s^{-1}
R. A. dynamical center (J2000)	03 33 36.35	h, m, s
Dec. dynamical center (J2000)	-36 08 25.8	$^{\circ}, ', ''$
$T_{\text{dyn}}(R_g = 1 \text{ kpc})$	3×10^7	yr
$M_{\text{dyn}}(R_g \leq 1 \text{ kpc})$	1×10^{10}	M_{\odot}
$M_{\text{mol}}/M_{\text{dyn}}(R_g \leq 1 \text{ kpc})$	0.1	
mean $R_{12/13}^{(2-1)}$	8.7	
r.m.s. $R_{12/13}^{(2-1)}$	2.8	
$\Sigma_{\text{mol}}/\Sigma_{\text{SFR}}(R_g \leq 1 \text{ kpc})$	1×10^8	yr

NOTE. — Parameters related to gas mass are derived from $^{12}\text{CO}(2-1)$ data using $N(\text{H}_2)/I_{\text{CO}(2-1)} = 0.5 \times 10^{20} \text{ cm}^{-2} (\text{K km s}^{-1})^{-1}$ and a factor of 1.36 for helium. See text for other assumptions and methods used to derive the parameters, and for their uncertainties.

TABLE 4
ASSOCIATION OF CO PEAKS WITH KNOWN SOURCES

sources			association with a CO peak						source parameters		
radio (1)	mid-IR (2)	optical (3)	I_{12} (4)	$T_{\text{b},12}$ (5)	I_{13} (6)	$T_{\text{b},13}$ (7)	I_{18} (8)	$T_{\text{b},18}$ (9)	$S_{3.5 \text{ cm}}$ (10)	$S_{11.9 \mu\text{m}}$ (11)	m_{B} (12)
Nuc.	M1	Nucleus	N	N	N	N	N	N	0.24	510 ± 100	17.00
A	...	SSC 10	N	N	N	N	N	N	0.97	...	21.42
...	M2	SSC 6	N	N	N	N	N	N	...	< 20	17.21
...	M3	SSC 3	N	N	N	N	N	N	...	30 ± 6	17.20
D	M4	... ^a	Y	Y	Y	Y	N	Y	1.47	40 ± 8	...
E	M5	... ^b	Y	Y	Y?	Y	N	N	0.80	120 ± 20	...
F	Y?	Y?	N	N	N	N	0.63
G	M6	...	Y	Y	Y	Y	N	Y?	1.56	140 ± 20	...
...	M7	...	N	N	N	N	N	N
H	M8?	...	Y	Y	N	Y	N	N	0.58
J	N	N	N	N	N	N	0.37

NOTE. — Col. (1) Radio sources (Sandqvist et al. 1995; Forbes & Norris 1998). Col. (2) Mid-IR sources (Galliano et al. 2005). M1 is the nucleus. Col. (3) Optical sources (Kristen et al. 1997). Cols. (4)–(9) Association with a peak in integrated intensity (I) and with a peak in brightness temperature (T_{b}). The subscripts 12, 13, and 18 indicate $^{12}\text{CO}(2-1)$, $^{13}\text{CO}(2-1)$, and $\text{C}^{18}\text{O}(2-1)$, respectively. Col. (10) Flux density in mJy at 3.5 cm (Stevens et al. 1999). The numbers here differ from those in Table 6 because of the different methods used to estimate and subtract the background. Col. (11) Flux density in mJy in the ‘11.9 μm filter’ of Galliano et al. (2005). Col. (12) B magnitude (Kristen et al. 1997).

^aGalliano et al. (2005) pointed out a conical feature near M4 in a HST image. See Fig. 3.

^bGalliano et al. (2005) pointed out a double source near M5 in a HST image. See Fig. 3.

TABLE 5
PROPERTIES OF CO HOTSPOTS WITH A RADIO COUNTERPART

R.A. (1)	Dec. (2)	velocity (3)	max T_b ,12 (4)	I_{12} (5)	ΔV_{12} (6)	$T_{b,12}/T_{b,13}$ (7)	I_{12}/I_{13} (8)	association (9)
36 ^h 39	18 ^m 7	1560	12.7	42	70	7.3 ± 0.6	7.7 ± 0.5	D, M4
36 ^h 61	16 ^m 0	1540	13.3	34	60	7.8 ± 0.7	9.3 ± 0.8	E, M5
36 ^h 77	18 ^m 5	1480	10.2	33	80	5.5 ± 0.4	8.1 ± 0.7	G, M6
36 ^h 76	23 ^m 6	1510	10.5	32	70	9.9 ± 1.4	11.2 ± 1.3	H, M8?
36 ^h 64	28 ^m 0	1590	9.8	37	90	12.9 ± 2.2	14.3 ± 1.7	F

NOTE. — Cols. (1)–(2) Position. $\alpha=0^h33^m$, $\delta=-36^\circ08'$ (J2000.0). Peak positions measured in the peak temperature maps of ^{12}CO and ^{13}CO are averaged for the CO hotspots corresponding to D,E,G, and H. The radio position is used for F. Col. (3) Velocity at which the peak brightness temperature of $^{12}\text{CO}(2-1)$ emission is observed. The unit is km s^{-1} . Columns from (3) to (6) are measured in the data cubes of $2.''6 \times 1.''8 \times 10 \text{ km s}^{-1}$ resolution. Col. (4) Peak brightness temperature of $^{12}\text{CO}(2-1)$ emission in K. Col. (5) Integrated $^{12}\text{CO}(2-1)$ intensity in the units of $\text{Jy km s}^{-1} \text{ arcsec}^{-2}$. Col. (6) Full width at half maximum of the $^{12}\text{CO}(2-1)$ line. The unit is km s^{-1} . Col. (7) Ratio of $^{12}\text{CO}(2-1)$ to $^{13}\text{CO}(2-1)$ brightness temperature at the velocity where $^{12}\text{CO}(2-1)$ has the maximum intensity. The ratios in this and the next columns are measured in $3.''3 \times 2.''0 \times 20 \text{ km s}^{-1}$ resolution cubes made using visibilities in the same $u-v$ range. The error is 1σ . Col. (8) Ratio of $^{12}\text{CO}(2-1)$ to $^{13}\text{CO}(2-1)$ integrated brightness temperatures and its 1σ error. Col. (9) Spatial association with sources in other wavelengths. D through H are radio sources (Sandqvist et al. 1995; Forbes & Norris 1998) and M# are mid-IR sources (Galliano et al. 2005).

TABLE 6
CO HOTSPOT – CLUSTER ASSOCIATIONS

	NGC 1365	Antennae	M83	(unit)
distance ^a	17.9	21.5	4.5	Mpc
$\log L_{8-1000 \mu\text{m}}^a$	11.00	10.84	10.29	L_\odot
name(s)	D/M4,E/M5,G/M6	WS95-80/SGMC4-5 ^b	M83-2 ^c	
$S_{3.5 \text{ cm}}$	1.8–4.2 ^d	4.7 ^e	4.8 ^f	mJy
$P_{3.5 \text{ cm}}$	0.7–1.5	2.6	0.11	$10^{20} \text{ W Hz}^{-1}$
$S_{11.9 \mu\text{m}}$	40–140	70 ^g	$\sim 1000^h$	mJy
$P_{11.9 \mu\text{m}}$	15–54	39	~ 24	$10^{20} \text{ W Hz}^{-1}$
max $T_b(\text{CO})^i$	10–13	4	11	K
$\max[\int T_b(\text{CO})dv]^j$	9–11	3	7	10^2 K km s^{-1}
Σ_{mol}^k	1.9–2.4	0.7	1.5	$10^3 x_{\text{CO}} M_\odot \text{ pc}^{-2}$
$\theta_{\text{CO beam}}^l$	1.8	4.1	0.7	10^2 pc

^aThe galaxy distances and luminosities are from Sanders et al. (2003), except that M83's distance is from Thim et al. (2003) and its luminosity is scaled for the distance.

^bThe names are from Whitmore & Schweizer (1995) and Wilson et al. (2000). The latter lists other names of the source.

^cIn Table 2 of Turner & Ho (1994).

^dThese flux densities are measured from the 3.5 cm map of Morganti et al. (1999). The spatial resolution of the data is $1.''6 \times 0.''8$. High-pass filtering is made for background subtraction using the AIPS task MWFLT with a $4.''5 \times 4.''5$ filtering box, to be consistent with the Antennae data.

^eThe flux density of the source reported in Neff & Ulvestad (2000). A $1.''4 \times 1.''0$ resolution image was used after high-pass filtering.

^fInterpolated from the 2 cm and 6 cm data in Turner & Ho (1994). The data resolution is $2.''5 \times 1.''6$. No background subtraction is made and the source is assumed to be unresolved.

^gFlux in a $6''$ pixel on the source (Mirabel et al. 1998; Wilson et al. 2000).

^hFlux in a $4''$ pixel on the source (Telesco et al. 1993).

ⁱPeak excess brightness temperature of ^{12}CO emission. The transition of CO is J=2–1 for NGC 1365 and M83 and J=1–0 for the Antennae. The Antenna data are from Wilson et al. (2000) and M83 data from Sakamoto et al. (2004).

^jIntegrated ^{12}CO intensity.

^kPeak surface density of molecular gas at the CO hotspot. It is estimated from the peak CO integrated intensity. Correction for inclination has not been made.

^lResolution of the CO data, i.e., the FWHM of the observing beam at the distance of the galaxy.

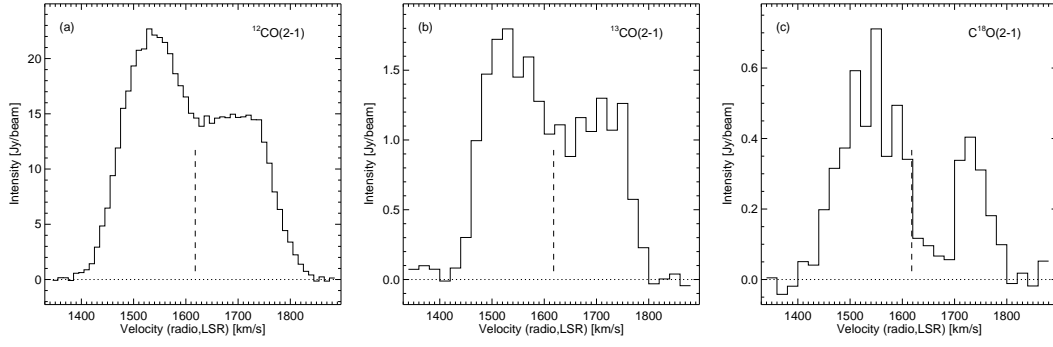


FIG. 1.— Spectra of ^{12}CO , ^{13}CO , and C^{18}O ($J=2-1$) emission in the central $25''$ of NGC 1365. For these spectra, the SMA data cubes also used for Fig. 2 are first corrected for primary beam attenuation, then convolved to a resolution of $25''$ (FWHM), and sampled at the galactic center position of Sandqvist et al. (1982), which was used in many single-dish observations. The dashed line shows the systemic velocity of the galaxy, $V_{\text{sys}}(\text{radio, LSR}) = 1618 \text{ km s}^{-1}$.

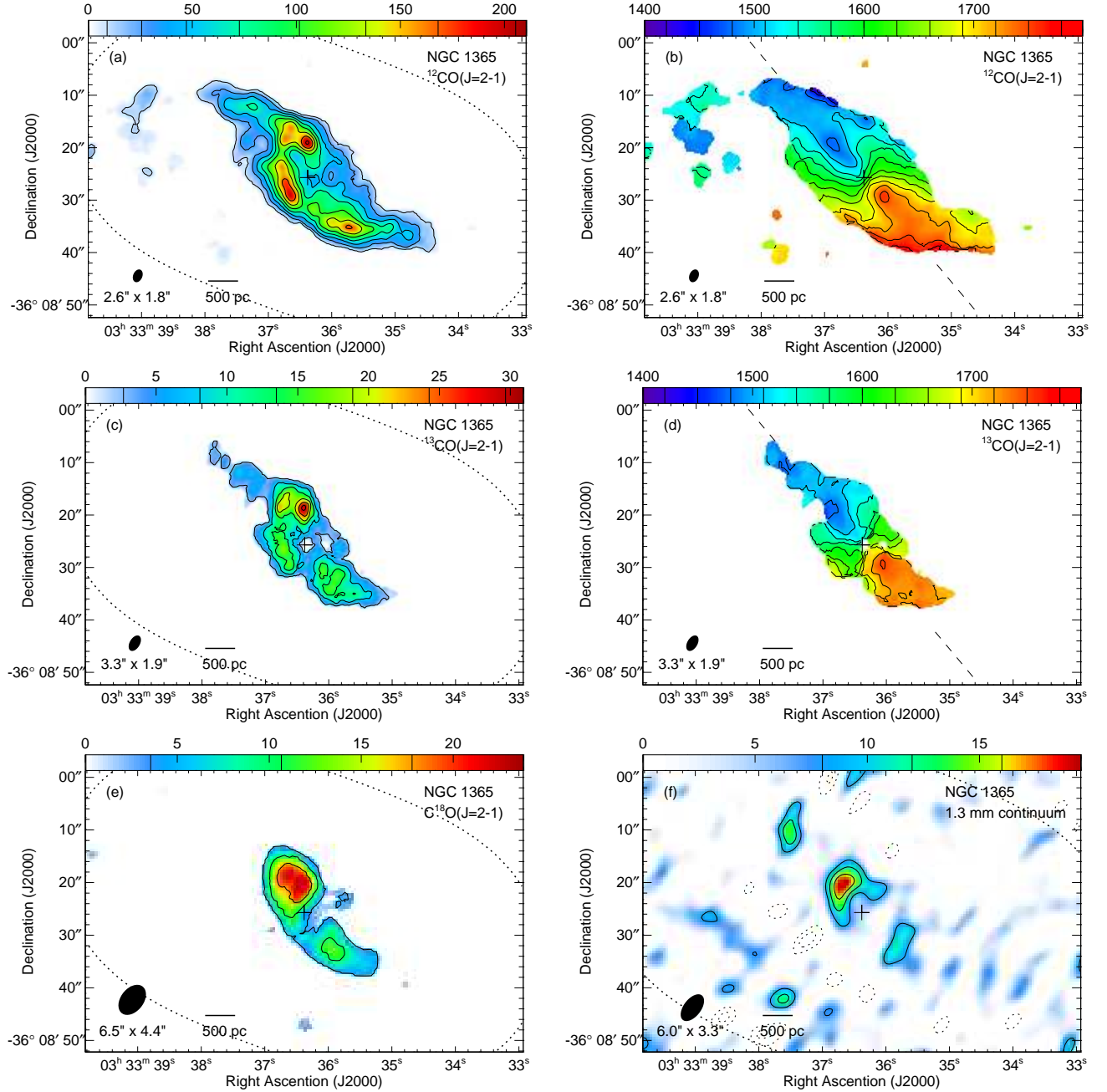


FIG. 2.— CO line and continuum images of the center of NGC 1365. (a) $^{12}\text{CO}(J=2-1)$ integrated intensity map. The n -th contour is at $9.1 \times n^{1.5}$ $\text{Jy beam}^{-1} \text{ km s}^{-1}$. (b) Mean velocity map of the $^{12}\text{CO}(J=2-1)$ emission. Contours are in 30 km s^{-1} steps. (c) $^{13}\text{CO}(J=2-1)$ integrated intensity map. Contours are at $2.7 \times [1, 3, 5, 7, 9, 11]$ $\text{Jy beam}^{-1} \text{ km s}^{-1}$. (d) Mean velocity map of the $^{13}\text{CO}(J=2-1)$ emission. Contours are at $3.6 \times [1, 3, 5]$ $\text{Jy beam}^{-1} \text{ km s}^{-1}$. (e) $\text{C}^{18}\text{O}(J=2-1)$ integrated intensity map. Contours are at $[-3, -2, 2, 3, 4] \times 4.0 \text{ mJy beam}^{-1}$ ($= 1\sigma$). Negative contours are dashed. The cross at the center of each image marks the active nucleus. The FWHM of the synthesized beam and a 500 pc scale are at the bottom left corner of each image. The dotted oval shows the mosaicked primary beam at its 50% level. The dashed line in the velocity maps is the line of nodes (P.A. = 220°).

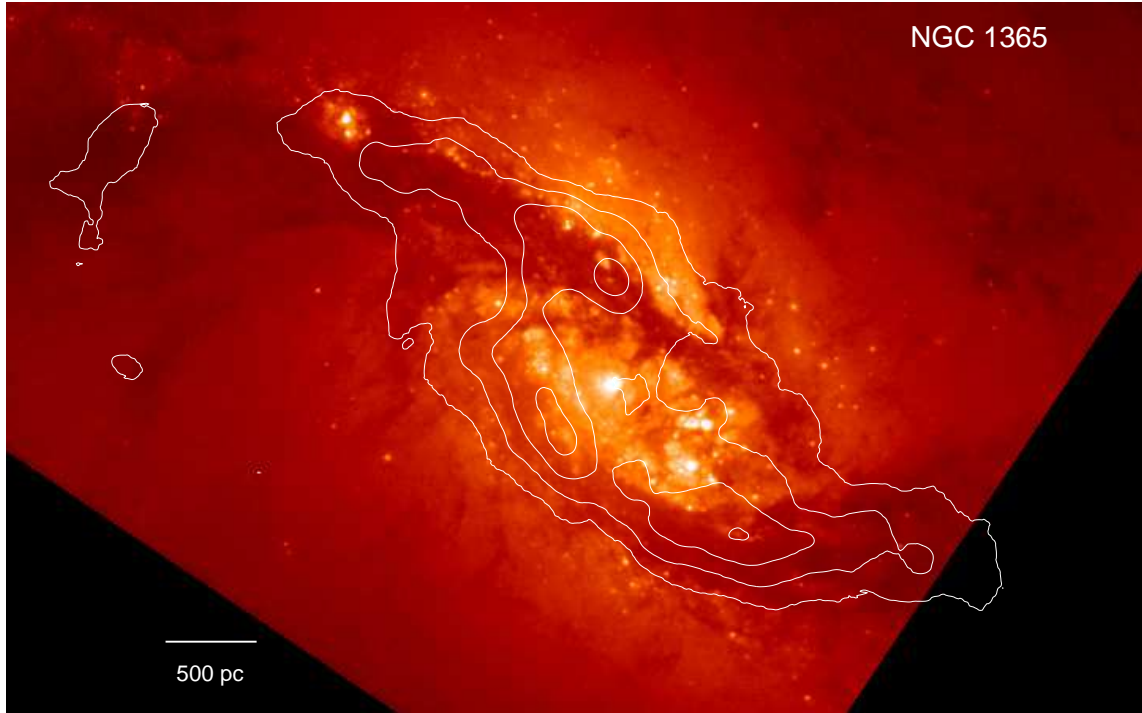


FIG. 3.— ^{12}CO contours on an archival HST image taken with the F606W filter. Every 2nd contour in Fig. 2 (a) is plotted on the logarithmically-scaled optical image. North is up, east is to the left. The HST image is shifted east by $1''.0$ from its header position to place the nucleus on its radio position.

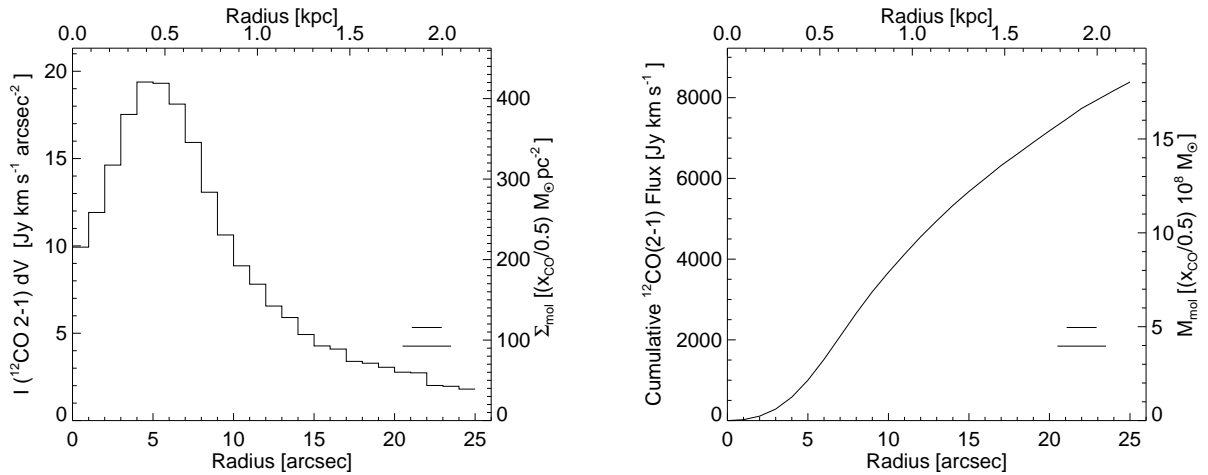


FIG. 4.— Radial distribution of $^{12}\text{CO}(2-1)$ emission around the galactic center measured in concentric circular annuli or circles in the galaxy plane. (left) The mean integrated intensities on the sky plane. The right axis is molecular gas surface density corrected for the inclination of the galaxy. (right) The cumulative flux of $^{12}\text{CO}(2-1)$ emission as a function of galactocentric radius. The right axis is the mass of molecular gas in units of $10^8 M_{\odot}$. Both plots are from the dataset of $2''.6 \times 1''.8$ resolution. See §4.1 for the conversion of ^{12}CO data to gas surface density and gas mass. The two horizontal bars in each plot show FWHM of the elliptical beam along the galaxy's major axis (upper bar) and the minor axis (lower bar). The lengths of both bars are calculated in the galaxy plane.

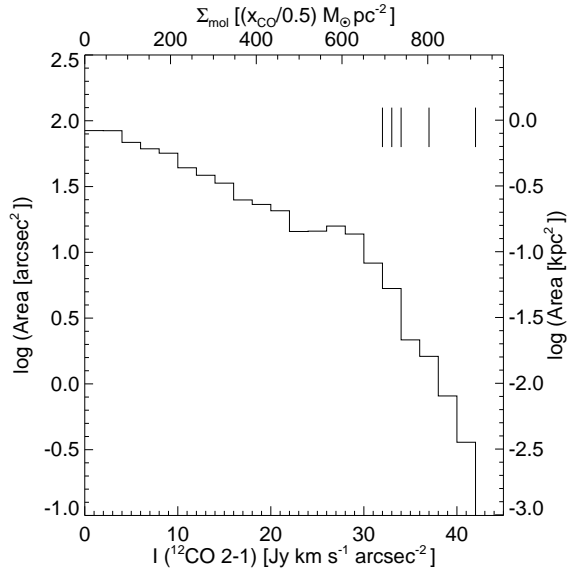


FIG. 5.— Histogram of $^{12}\text{CO}(2-1)$ integrated intensity within 2.5 kpc of the nucleus in the galaxy plane. The vertical lines in the upper right mark the data for the CO hotspots in Table 5. The moment map with $2''.6 \times 1''.8$ resolution was used for this plot after corrected for the mosaicked primary beam. The area covered by the synthesized beam is 5.1 arcsec^2 on the sky and $5.1 \times 10^{-2} \text{ kpc}^2$ on the galaxy plane. The top axis is the inclination-corrected surface density of molecular gas (Σ_{mol}) in units of $M_{\odot} \text{pc}^{-2}$. See §4.1 for the mass estimate from CO flux. The left axis is the surface area in the galaxy plane. Multiply the bottom axis by 1.3 to obtain the total visual extinction in our line of sight in mag for $N(\text{H}_2)/A_V = 1 \times 10^{21} \text{ cm}^{-2} \text{ mag}^{-1}$.

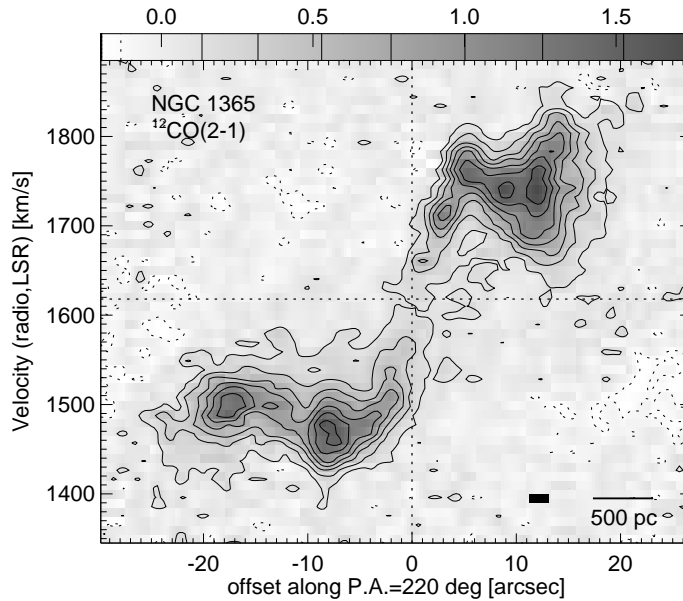


FIG. 6.— Position-velocity diagram of $^{12}\text{CO}(2-1)$ emission along the line of nodes. The n -th solid contour is at $n^{1.25} \times 134 \text{ mJy beam}^{-1}$; the lowest contour is at 2σ . Negative contours are dashed and have the same absolute values as positive ones. Conversion to brightness temperature in K can be made by multiplying by 5.2. The diagram is corrected for the mosaicked primary beam. The abscissa is measured from the active nucleus. The horizontal dotted line indicates the systemic velocity of 1618 km s^{-1} . The black rectangle at the bottom right corner represents a resolution element.

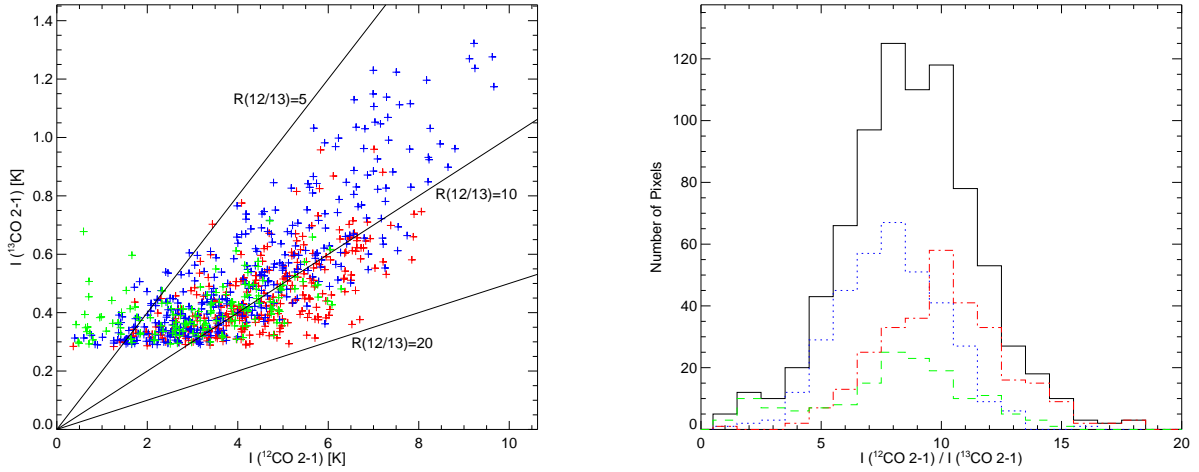


FIG. 7.— (left) Comparison of $^{12}\text{CO}(2-1)$ and $^{13}\text{CO}(2-1)$ line intensities in the center of NGC 1365. The line intensities are sampled from data cubes of matching spatial and velocity resolutions, $3''.3 \times 2''.0$ and 20 km s^{-1} . The sampling spacing is $1''.2$. Only those points where both lines are detected above 3σ are plotted. The 1σ noise is 0.12 K and 0.09 K for $^{12}\text{CO}(2-1)$ and $^{13}\text{CO}(2-1)$, respectively, at the center of the mosaics. The noise varies across the maps corrected for primary beam, and so does the cutoff threshold in kelvin. (right) Histogram of $^{12}\text{CO}(2-1)$ to $^{13}\text{CO}(2-1)$ intensity ratio. The one in black is from the entire data. The blue and red ones are from the near and far side, respectively, and within the galactocentric radius of 1 kpc ($= 12''$). Data from outside the circumnuclear disk are plotted in green.

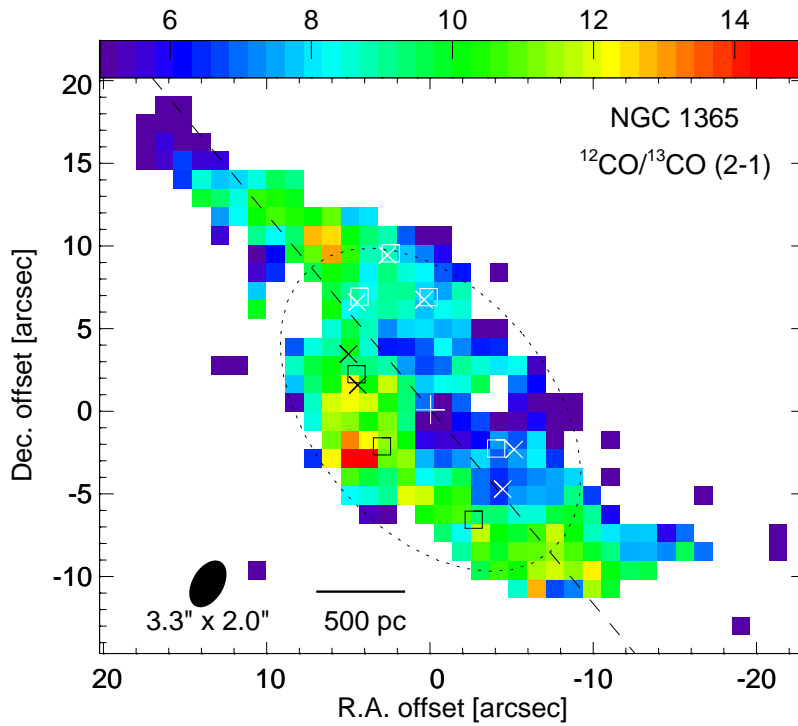


FIG. 8.— Spatial distribution of $^{12}\text{CO}(2-1)$ to $^{13}\text{CO}(2-1)$ brightness temperature ratio. Ratios of different velocities are averaged at each position. The + sign marks the active nucleus and the dashed line is the line of nodes; the near side is to the northwest. The dotted ellipse is at the galactocentric radius of 1 kpc ($= 12''$), and the boxes and crosses mark the radio and mid-IR sources, respectively, in Fig. 9.

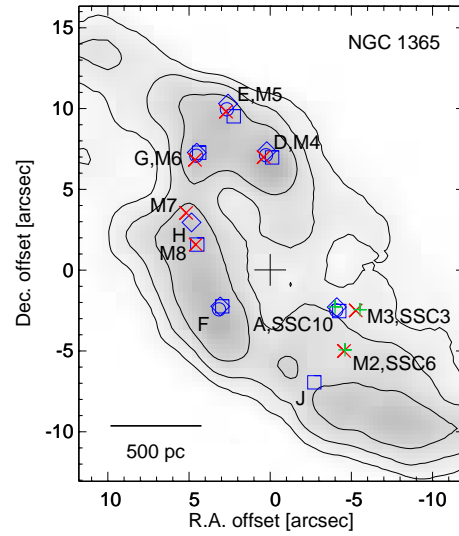


FIG. 9.— A guide map of radio, mid-IR, and optical sources in the center of NGC 1365. Sources A, D, E, F, G, H, and J are radio hotspots. Their positions are shown as diamonds (Sandqvist et al. 1995, $\lambda_{\text{obs}} = 2.6$ cm), squares (Stevens et al. 1999, $\lambda_{\text{obs}} = 3.5, 6$ cm), and circles (Thean et al. 2000, $\lambda_{\text{obs}} = 3.5$ cm). Sources M2 through M8 shown as X symbols are mid-IR sources of Galliano et al. (2005). Super star clusters (SSCs) 3, 6, and 10, shown with plus signs, are optically identified by Kristen et al. (1997). SSC 3 and SSC 6 are the two brightest ($M_B = -16.6$ mag) clusters in the region. Positions are measured with respect to the Seyfert nucleus; see Table 1 for its absolute coordinates. The background is our map of $^{12}\text{CO}(2-1)$ integrated intensity to guide the eyes.

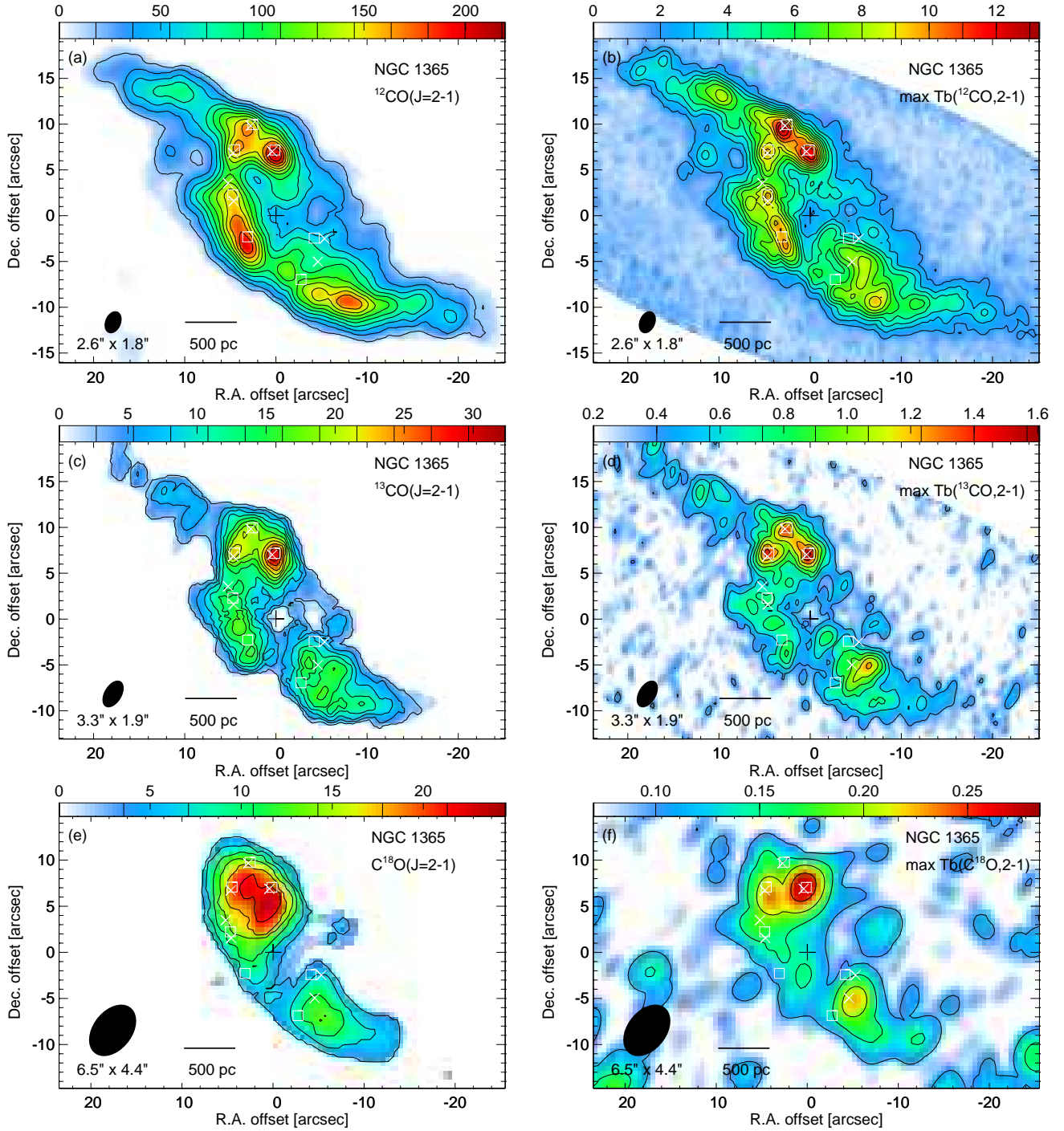


FIG. 10.— Radio and mid-IR sources plotted on the maps of CO integrated intensity (left) and peak brightness temperature (right). Squares are seven radio peaks observed in centimeter wavelengths (Stevens et al. 1999; Sandqvist et al. 1995; Thean et al. 2000) and crosses are mid-IR sources observed by Galliano et al. (2005). The background images are integrated intensities in $\text{Jy beam}^{-1} \text{ km s}^{-1}$ for the left column and brightness temperatures in K for the right. Each map is corrected for the primary beam attenuation. The + sign at the center of each image marks the galaxy nucleus. The synthesized beam and a 500 pc scale are at the bottom left corner of each panel.

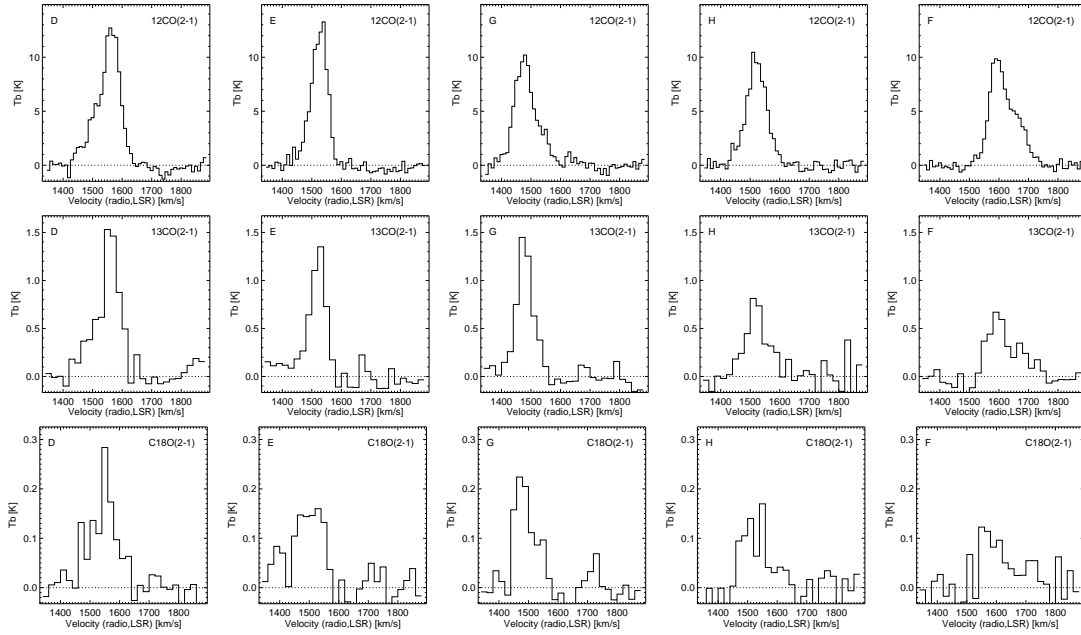


FIG. 11.— Spectra of CO hotspots. At the top of each panel are the radio name of the hotspot and the line name. The spectra are sampled from the data cubes used for Fig. 2 at the positions in Table 5 after primary-beam correction. Intensities are in brightness temperatures. The beam size, and hence the degree of beam dilution, are different for the three lines.

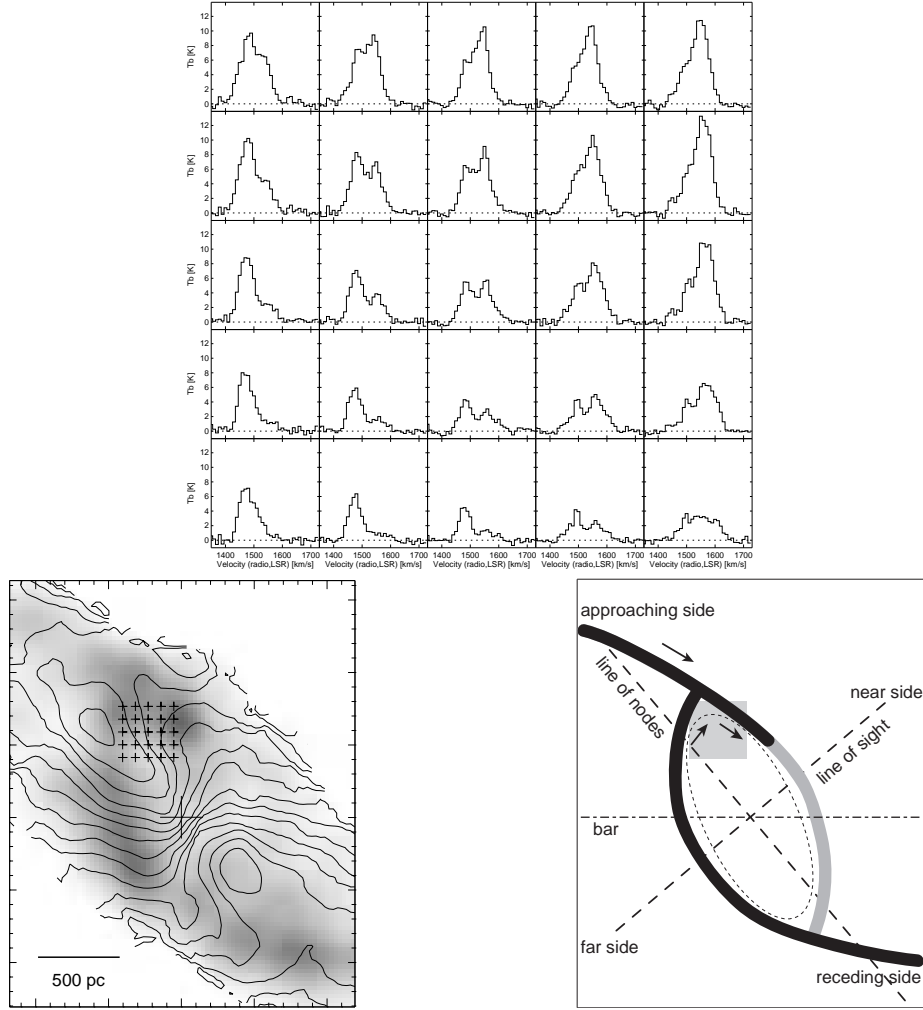


FIG. 12.— (a) Spectra of ^{12}CO near an apocenter of the circumnuclear ring. The double-peak profiles indicate the motion of gas roughly along the circumnuclear ring. (b) Sampling positions of the line profiles, shown as a group of small plus signs. The background image is the ^{12}CO integrated intensity, and the contours are the ^{12}CO mean velocity in 20 km s^{-1} steps. (c) Illustration of the gas motion. The double-peaked profiles in the sampling region (= the gray square) are due to the distinctively different velocities in our line of sight between the gas approaching on the ring to the apocenter and the gas leaving it along the ring. The gas streamline on the ring can be oval similar to the dotted ellipse, or it may have a cusp at a shock. In either case, its major axis makes an oblique angle with the stellar bar ($\lesssim 90^\circ$ measured in the direction of the galaxy rotation, or clockwise), indicating that the gas streamline is x_2 -like. Around the apocenter, the gas flow on the molecular ring and another flow roughly along a leading-edge gas lane on the bar (almost) converge, likely leading to frequent cloud collisions. The major and minor axes of the galaxy are shown as the dashed lines and the stellar bar as the dot-dashed line.

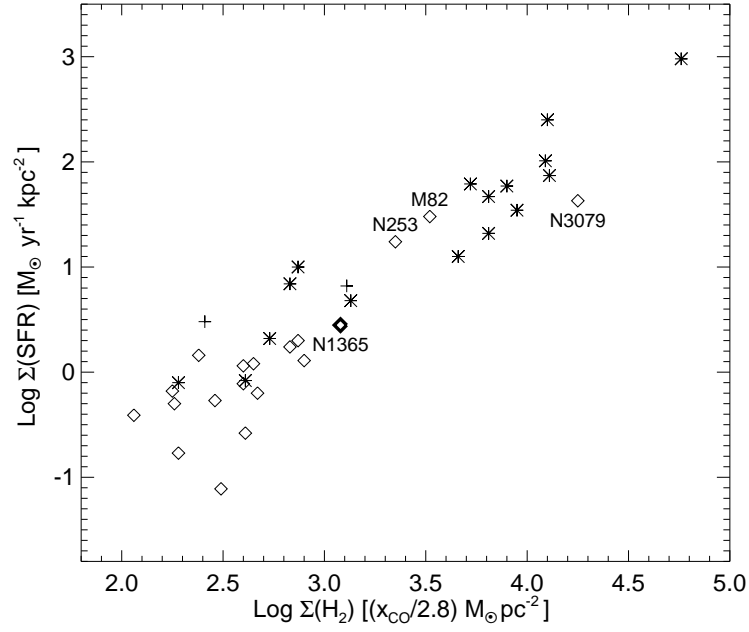


FIG. 13.— NGC 1365 in the Schmidt-law plot of Kennicutt (1998, Fig. 5) for starburst nuclei. The gas surface density and the star formation rate are averaged over the circumnuclear starburst region of each galaxy. The size of the starburst region is individually determined and is different for each galaxy. It is 2 kpc in diameter for NGC 1365 and is taken from K98 for others. The gas surface densities are normalized with $x_{\text{CO}} = 2.8$ only to make a fair comparison. Asterisks are mergers and diamonds are non-merging galaxies. The plus symbols are for two distant (> 100 Mpc) galaxies that are likely mergers judging from their large far-IR luminosities ($\log(L_{8-1000\mu\text{m}}/L_{\odot}) \geq 11.80$; Sanders et al. 2003) but lack morphological evidence for merging.